Asymptotic expansion and Padé approximants for acceleration-driven Poiseuille flow of a rarefied gas: Bulk hydrodynamics and rheology

Ramakrishna Rongali and Meheboob Alam

Phys. Rev. E **98**, 012115 — Published 13 July 2018

DOI: 10.1103/PhysRevE.98.012115

Asymptotic expansion and Padé-approximants for acceleration-driven Poiseuille flow of a rarefied gas: bulk hydrodynamics and rheology

Ramakrishna Rongali and Meheboob Alam*
Engineering Mechanics Unit,
Jawaharlal Nehru Centre for Advanced Scientific Research,
Jakkur P.O., Bangalore 560064, India
(Dated: June 29, 2018)

The perturbation expansion technique is employed to solve the Boltzmann equation for the acceleration-driven steady Poiseuille flow of a dilute molecular gas flowing through a planar channel. Neglecting wall-effects and focussing only on the bulk hydrodynamics and rheology, the perturbation solution is sought around the channel centerline in powers of the strength of acceleration. To make analytical progress, the collision term has been approximated by the Bhatnagar-Gross-Krook (BGK) kinetic model for hard-spheres, and the related problem for Maxwell molecules was analysed previously by Tij and Santos (J. Stat. Phys., 1994, vol. **76**, 1399-1415). The analytical expressions for hydrodynamic (velocity, temperature and pressure) and rheological fields (normal stress differences, shear viscosity and heat flux) are obtained by retaining terms up-to tenth-order in acceleration, with one aim of the present work being to understand the convergence properties of the underlying perturbation series solutions. In addition, various rarefaction effects (e.g. the bimodal shape of the temperature profile, non-uniform pressure profile, normal-stress differences, and tangential heat flux) are also critically analysed in the Poiseuille flow as functions of the local Froude number. The hydrodynamic and rheological fields evaluated at the channel centreline confirmed oscillatory nature of the present series solutions (when terms of increasing order are sequentially included), signalling the well-known pitfalls of asymptotic expansion. The Padé approximation technique is subsequently applied to check the region of convergence of each series solution. It is found that the diagonal Padé-approximants for rheological fields agree qualitatively with previous simulation data on acceleration-driven rarefied Poiseuille flow.

PACS numbers: 45.70.-n, 45.50.-j, 05.20.Dd, 51.10.+y

I. INTRODUCTION

The Poiseuille flow corresponds to the steady flow of a gas or liquid along a long channel of constant cross-section driven by an imposed pressure difference across the ends of the channel – this represents one of the well-known classical problems in fluid dynamics, first studied by Poiseuille [1] and Hagen [2] in the 19th century. During the last few decades, the Poiseuille flow of a molecular gas [3] has been analyzed by replacing the pressure difference by a constant external field, namely, the gravitational acceleration (see the schematic in Fig. 1) and has gotten much consideration from theoretical [4–15] analyses using both kinetic and hydrodynamic theory as well as via computational [16–21] approaches using "direct simulation Monte Carlo" (DSMC) and molecular dynamics (MD) methods [22]. The earliest kinetic theory analyses of Cercignani and Daneri [4], using the well-known BGK (Bhatnagar-Gross-Krook) kinetic model [23], resolved a half-century-old paradox ("Knudsen paradox" [3]): the mass flow rate ($Q = \int \rho(y) u_x(y) dy$, where $\rho(y)$ and $u_x(y)$ is the density and velocity of the gas across the channel width, see Fig. 1) decreases, reaches a minimum and finally increases slowly with increasing Knudsen number ($\mathrm{Kn} = \lambda/W$, the ratio between the mean free path and the channel width). Their analysis uncovered that the flow rate increases logarithmically ($Q \sim \log \mathrm{Kn}$) in the rarefied and free molecular regime (i.e. at $\mathrm{Kn} > 1$); on the other hand, the Navier-Stokes hydrodynamics (valid at small Kn) predicts a monotonic decay of flow rate ($Q \sim \mathrm{Kn}^{-1}$) with increasing Kn. After the successful resolution of Knudsen paradox, the kinetic theory has been increasingly used to analyse various unique characteristics of rarefied gases in different canonical flow configurations (Couette flow, Poiseuille flow, Fourier flow, Benard convection, etc.). In the context of Poiseuille flow, another landmark prediction of kinetic theory [5] is the finding of the "bimodal" shape of the temperature profile: the temperature of the gas has a local minimum at the channel center (T_0), with two symmetric maxima ($T_{\max}$) away from the centreline-minimum. The degree of temperature bimodality is quantified by the excess temperature

$$\Delta T = \frac{T_{\max} - T_0}{T_0}. \tag{1}$$

While the Navier-Stokes theory predicts $\Delta T = 0$ (i.e. the maximum temperture occurs at the channel centreline), the kinetic theory analysis of Tij and Santos [5] uncovered that $\Delta T \neq 0$ for $\mathrm{Kn} > 0$ and the transverse location of temperature maximum is predicted to be $y_{\max} \equiv y(T = T_{\max}) \approx 3\lambda$, where λ is the mean-free path of the gas. This theoretical prediction has later been verified by Mansour *et al.* [16] via DSMC simula-

* meheboob@jncasr.ac.in

tions. It has been established [5] that the appearance of a quadratic term in the temperature profile is responsible for the origin of temperature bimodality which is clearly a signature of the rarefaction (Kn > 0) of the gas; another related prediction is that the transverse pressure profile is non-uniform (i.e. $dp/dy \neq 0$) and is also charaterized by a local "minimum" or "dip" at the channel centerline: this can be understood from the equation of state $p = nT$ of an ideal gas by assuming that the density is nearly homogeneous along the transverse direction and hence a temperature-dip at the channel center would necessarily imply a pressure-dip at the same location. Other rarefaction-induced phenomena are (i) non-zero normal-stress differences

$$\mathcal{N}_1 = \frac{P_{xx} - P_{yy}}{p} \neq 0 \quad \text{and} \quad \mathcal{N}_2 = \frac{P_{yy} - P_{zz}}{p} \neq 0, \quad (2)$$

where $P = [P_{ij}]$ is the pressure tensor with $p = P_{ii}/3$ being the mean pressure, and (ii) a non-zero tangential heat flux

$$q_x \neq 0, \quad (3)$$

even though there is no temperature gradient along the tangential direction (x). Note that x, y and z denote the streamwise/tangential, transverse/normal and vorticity directions, respectively, see Fig. 1. A related puzzle in rarefied Poiseuille flow is tied to the normal component of the heat-flux: the heat flows from the channel centre towards the walls, even though the temperature maximum is located away from the centre – the Navier-Stokes-order theory is unable to explain this unusual effect in apparent contradiction to standard Fourier's law.

In this paper, we analyse the acceleration-driven Poiseuille flow of a dilute molecular gas in the framework of Boltzmann kinetic theory, following the earlier work of Tij and Santos [5] who analysed the same flow by considering Maxwell molecules in contrast to a hard-sphere gas in the present paper. The Boltzmann collision operator is approximated via a single relaxation time, and the resulting BGK kinetic model [23] is solved by using a perturbation expansion of the velocity distribution function in powers of the strength of gravitational acceleration by retaining terms up to tenth order. Analytical expressions have been derived for the hydrodynamic fields and their fluxes (pressure tensor and heat flux vector). These solutions are subsequently used to assess (i) the asymptotic nature of the perturbation expansion and (ii) the related convergence problem – these two issues were not considered in Ref. [5]. This constitutes the primary focus of the present work, and other goals are (i) to estimate the range of validity of the series solutions in terms of local Froude number and (ii) analyse the temperature bimodality, normal stress differences, shear viscosity and heat flux using presently obtained high-order series solutions. It is found that the excess temperature ΔT, Eq. (1), shows oscillating behaviour with Froude numbers with the addition of higher-order terms in the series solution; such oscillatory behaviour is also replicated in the solutions for normal stress differences, shear viscosity and heat flux. A detailed analysis of all transport coefficients at the channel centreline is carried out; the related power-series expressions (in terms of the centerline Froude number Fr_0) clearly reveal the origin of the underlying oscillatory behaviour of each series-solution with Fr_0. The Padé approximation method is subsequently employed to check the convergence properties of the series solutions for rheological fields.

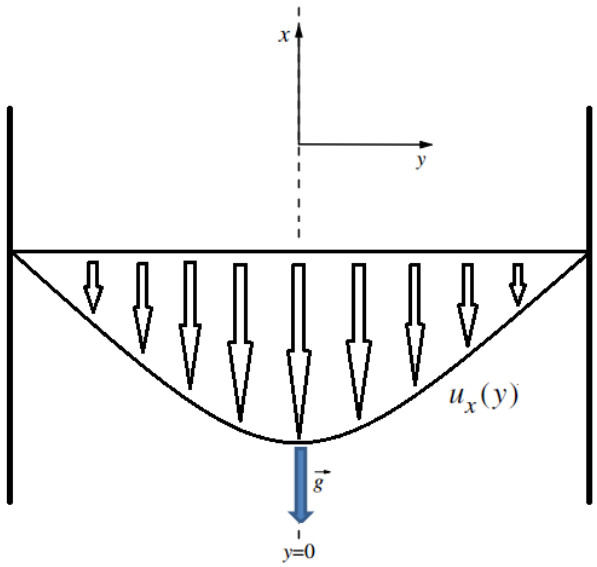

FIG. 1. Schematic of the gravity-driven planar Poiseuille flow. The flow is directed along the negative x-direction, driven by the gravitational acceleration (g). Two planar walls are placed at $y = \pm W/2$, with W being much much larger than the mean free path of the gas such that the wall-effects can be neglected as assumed in the present analysis. The direction normal to the flow plane (x, y) is referred to as z-direction.

II. KINETIC THEORY AND ACCELERATION-DRIVEN POISEUILLE FLOW

In kinetic theory description, the state of a dilute gas can be specified by the single-particle distribution function $f(\boldsymbol{x}, \boldsymbol{c}; t)$ which characterizes the spatial and velocity distribution of individual particles – all relevant macroscopic properties of the gas can be obtained via coarse-graining of $f(\boldsymbol{x}, \boldsymbol{c}; t)$ over velocity space. The time evolution of single-particle distribution $f(\boldsymbol{x}, \boldsymbol{c}; t)$ obeys the Boltzmann equation which is the master equation in the kinetic theory of rarefied gases derived by Ludwig Boltzmann in 1872. The Boltzmann equation for single-particle velocity distribution function $f(\boldsymbol{x}, \boldsymbol{c}; t)$ in the dilute regime reads

$$\left(\partial_t + \boldsymbol{c} \cdot \boldsymbol{\nabla} + \boldsymbol{g} \cdot \frac{\partial}{\partial \boldsymbol{c}}\right) f = J[f, f], \quad (4)$$

where $\boldsymbol{g}$ is the gravitational acceleration and $J[f,f]$ is the collision operator, which measures the rate of change of the distribution function due to binary collisions. Adopting Boltzmann's molecular chaos ansatz, the explicit form of collision operator for hard-spheres is given by

$$J[f,f] = \sigma^2 \int d\boldsymbol{c}_1 \int d\hat{\boldsymbol{\sigma}}\ \mathcal{H}(\boldsymbol{c}_{01}\cdot\hat{\boldsymbol{\sigma}})(\boldsymbol{c}_{01}\cdot\hat{\boldsymbol{\sigma}}) \\ [f(\boldsymbol{c}'')f(\boldsymbol{c}_1'') - f(\boldsymbol{c})f(\boldsymbol{c}_1)], \quad (5)$$

where $\mathcal{H}(\cdot)$ represents the Heaviside step function, $\hat{\boldsymbol{\sigma}}$ is a unit vector directed along the center of the particle without index to the particle with index 1 at contact, $\boldsymbol{c}_{01} = \boldsymbol{c} - \boldsymbol{c}_1$ is the post-collisional relative velocity. The pre-collisional velocities $\boldsymbol{c}''$ and $\boldsymbol{c}_1''$ are given in terms of post-collisional velocities $\boldsymbol{c}$ and $\boldsymbol{c}_1$ via the following collision rules:

$$\boldsymbol{c}'' = \boldsymbol{c} - (\boldsymbol{c}_{01}\cdot\hat{\boldsymbol{\sigma}})\hat{\boldsymbol{\sigma}} \quad \text{and} \quad \boldsymbol{c}_1'' = \boldsymbol{c}_1 + (\boldsymbol{c}_{01}\cdot\hat{\boldsymbol{\sigma}})\hat{\boldsymbol{\sigma}}. \quad (6)$$

The macroscopic fields, namely, the number density n, the flow velocity $\boldsymbol{u}$ and the temperature T are defined as the zeroth, first and second moments of the distribution function, respectively, given by

$$\begin{pmatrix} n(\boldsymbol{x},t) \\ n(\boldsymbol{x},t)\ \boldsymbol{u}(\boldsymbol{x},t) \\ n(\boldsymbol{x},t)\ k_B\ T(\boldsymbol{x},t) \end{pmatrix} = \int d\boldsymbol{c} \begin{pmatrix} 1 \\ \boldsymbol{c} \\ \frac{m}{3}C^2 \end{pmatrix} f(\boldsymbol{x},\boldsymbol{c};t), \quad (7)$$

where $\boldsymbol{C} = \boldsymbol{c} - \boldsymbol{u}$ is the peculiar velocity, m is the mass of a particle and k_B is the Boltzmann constant which is set to unity. The transport equations for the hydrodynamic variables are obtained by taking appropriate velocity moments of Eq. (4):

$$\left(\frac{\partial}{\partial t} + \boldsymbol{u}\cdot\boldsymbol{\nabla}\right) n = -n\boldsymbol{\nabla}\cdot\boldsymbol{u}, \quad (8)$$

$$\left(\frac{\partial}{\partial t} + \boldsymbol{u}\cdot\boldsymbol{\nabla}\right) \boldsymbol{u} = -\frac{1}{\rho}\boldsymbol{\nabla}\cdot\boldsymbol{P} + \boldsymbol{g}, \quad (9)$$

$$\frac{3}{2}n\left(\frac{\partial}{\partial t} + \boldsymbol{u}\cdot\boldsymbol{\nabla}\right) T = -\boldsymbol{\nabla}\cdot\boldsymbol{q} - \boldsymbol{P}:\boldsymbol{\nabla}\boldsymbol{u}, \quad (10)$$

representing conservation of mass, momentum and energy, respectively. Note that

$$\rho(\boldsymbol{x},t) = mn(\boldsymbol{x},t) = m\int d\boldsymbol{c} f(\boldsymbol{x},\boldsymbol{c};t) \quad (11)$$

is the mass density,

$$\boldsymbol{P}(\boldsymbol{x},t) = m\int d\boldsymbol{c}\ \boldsymbol{C}\boldsymbol{C} f(\boldsymbol{x},\boldsymbol{c};t) \quad (12)$$

is the pressure tensor, and

$$\boldsymbol{q}(\boldsymbol{x},t) = \frac{m}{2}\int d\boldsymbol{c}\ C^2\boldsymbol{C} f(\boldsymbol{x},\boldsymbol{c};t) \quad (13)$$

is the heat flux vector.

A. Gravity-driven Poiseuille flow of a molecular gas

Here we consider the "acceleration-driven" Poiseuille flow confined in a planar channel geometry as depicted schematically in Fig. 1– the molecular gas, composed of a collection of hard-spheres of diameter σ (and mass m), is enclosed between two infinite parallel plates normal to the y-axis. A constant external force per unit mass (e.g., gravity) $\boldsymbol{g} = -g\hat{\boldsymbol{x}}$ is applied along the $\boldsymbol{x}$-direction. As will be clarified later, our analysis is restricted to the "bulk-region" of the channel around its mid-plane ($y = 0$) since we do not incorporate wall-effects in the present analysis. The underlying assumption is that the bounding walls are placed at $y = \pm W/2$, with W being much much larger than the mean free path of the gas such that the wall-effects on the flow-behaviour in the bulk can be neglected.

A steady fully developed flow can be expected in which the hydrodynamic quantities depend only on the transverse coordinate y and the flow velocity is parallel to the x-axis, i.e.,

$$\boldsymbol{u} = u_x(y)\hat{\boldsymbol{x}}. \quad (14)$$

Under the assumptions of steady $[\partial/\partial t(\cdot) = 0]$ and fully developed flow

$$\frac{\partial}{\partial y}(\cdot) \neq 0, \quad \text{but} \quad \frac{\partial}{\partial x}(\cdot) = 0 = \frac{\partial}{\partial z}(\cdot), \quad (15)$$

the Boltzmann equation (4) takes the following form

$$\left(-g\frac{\partial}{\partial c_x} + c_y\frac{\partial}{\partial y}\right) f = J[f,f]. \quad (16)$$

Similarly, the mass balance equation [Eq. (8)] is identically satisfied, and the remaining conservation equations for momentum [Eq. (9)] and energy [Eq. (10)] reduce to

$$\frac{dP_{yy}}{dy} = 0, \quad \frac{dP_{yx}}{dy} = -\rho g, \quad P_{yx}\frac{du_x}{dy} + \frac{dq_y}{dy} = 0. \quad (17)$$

We need to solve Eq. (16) analytically/perturbatively, supplemented by related hydrodynamic equations (17) for the acceleration-driven planar Poiseuille flow. To make analytical progress, we use an approximate expression for the collision operator $J[f,f]$, Eq. (5), as described below.

B. Kinetic model

To avoid the intricacies in the subsequent perturbation analysis, we employ the well-known BGK kinetic model [23] for the Boltzmann equation. In this model the collision operator $J[f,f]$ is replaced by a single-time relaxation term of the form

$$J[f,f] \to -\nu(f - f_M), \quad (18)$$

where ν is the collision frequency

$$\nu = \frac{16\sqrt{\pi}}{5} n\sigma^2 \sqrt{\frac{T}{m}}, \tag{19}$$

and f_M is the local Maxwellian distribution

$$f_M(\boldsymbol{x}, \boldsymbol{c}; t) = n(\boldsymbol{x}, t)\left[\frac{m}{2\pi k_B T(\boldsymbol{x}, t)}\right]^{3/2} \times \exp\left[-\frac{m(\boldsymbol{c} - \boldsymbol{u}(\boldsymbol{x}, t))^2}{2k_B T(\boldsymbol{x}, t)}\right]. \tag{20}$$

The Navier-Stokes-level shear viscosity (η) and thermal conductivity (κ) derived from the BGK kinetic model can be expressed in terms of the collision frequency[24]:

$$\eta = \frac{p}{\nu} \quad \text{and} \quad \kappa = \frac{5}{2}\frac{p}{m\nu}. \tag{21}$$

With the help of Eq. (18), the kinetic equation (16) reads

$$\left(-g\frac{\partial}{\partial c_x} + c_y\frac{\partial}{\partial y}\right) f = -\nu(f - f_M). \tag{22}$$

In the remainder of this paper, the above equation will be solved, in conjunction with related hydrodynamic equations Eq. (17), using perturbation expansion.

III. SOLUTION VIA PERTURBATION EXPANSION

The non-equilibrium distribution function can be written as

$$f = f_M(1 + \Phi), \tag{23}$$

where Φ is its deviation from the local Maxwellian. Substituting Eq. (23) into Eq. (22) we obtain

$$(1+\Phi)\left[C_y\widetilde{\partial}_y \log f_M - \left(g + C_y\frac{\partial u_x}{\partial y}\right)\frac{\partial}{\partial C_x}\log f_M\right] = \left(g + C_y\frac{\partial u_x}{\partial y}\right)\frac{\partial \Phi}{\partial C_x} - C_y\widetilde{\partial}_y\Phi - \nu\Phi, \tag{24}$$

where the operator $\widetilde{\partial}_y$ is defined via

$$\widetilde{\partial}_y \equiv \frac{\partial}{\partial y} + \left(\frac{\partial u_x}{\partial y}\right)\frac{\partial}{\partial C_x}. \tag{25}$$

Since we are interested about the solution of Eq. (24) in the "bulk" region (around the centerline of the channel, see Fig. 1), it is convenient to use the state at the channel center $y = 0$ as a reference state. The following dimensionless quantities are introduced:

$$\boldsymbol{C}^* = \frac{\boldsymbol{C}}{c_0},\ \ y^* = \frac{y\nu_0}{c_0},\ \ f_M^* = \frac{f_M c_0^3}{n_0},\ \ \boldsymbol{u}^* = \frac{\boldsymbol{u}}{c_0},\ \ T^* = \frac{T}{T_0},\ \ \nu^* = \frac{\nu}{\nu_0},\ \ \boldsymbol{P}^* = \frac{\boldsymbol{P}}{p_0},\ \ \boldsymbol{q}^* = \frac{\boldsymbol{q}}{p_0 c_0} \tag{26}$$

where the subscript 0 denotes quantities evaluated at $y = 0$, and

$$c_0 = \sqrt{\frac{2k_B T_0}{m}} \tag{27}$$

is the centreline thermal speed. The important parameter is the dimensionless gravitational acceleration

$$g^* = \frac{g}{\nu_0 c_0} \tag{28}$$

which measures the strength of the gravity field on a particle moving with the thermal-speed along a distance of the order of the mean free path, while $y^* = y\nu_0/c_0$ is the dimensionless distance in units of local mean free path. In terms of non-dimensional units defined in Eq. (26), the kinetic equation Eq. (24) can be written as

$$(1+\Phi)\left[c_y^*\widetilde{\partial}_{y^*}\log f_M^* + \frac{2(c_x^* - u_x^*)}{T^*}\left(g^* + c_y^*\frac{\partial u_x^*}{\partial y^*}\right)\right] = \left(g^* + c_y^*\frac{\partial u_x^*}{\partial y^*}\right)\frac{\partial\Phi}{\partial c_x^*}\Phi - c_y^*\widetilde{\partial}_{y^*}\Phi - \nu^*\Phi, \tag{29}$$

where

$$\widetilde{\partial}_{y^*}\log f_M^* = \frac{\partial \log p^*}{\partial y^*} + \left(\frac{{C^*}^2}{T^*} - \frac{5}{2}\right)\frac{\partial \log T^*}{\partial y^*}. \tag{30}$$

For convenience, the asterisks will be dropped in the subsequent analysis, and all the quantities will be understood to be expressed in dimensionless units via Eq. (26).

A. Perturbation Expansion

To solve Eq. (29), a perturbation expansion of Φ in powers of the dimensionless gravitation acceleration $g = g^*$ is assumed [5]:

$$\Phi = \sum_{\alpha=1}^{n} \Phi^{(\alpha)} g^\alpha + O(g^{n+1}). \tag{31}$$

Recall that, in the absence of gravity, the solution to Eq. (22) is $f = f_M$ and hence $\Phi \equiv 0$ at $g = 0$, corresponding to an equilibrium gas with constant n, T, p and $\boldsymbol{u}$. We have determined solutions up-to tenth-order $O(g^{10})$, and hence the expansions for the hydrodynamic field variables can be written as

$$p = 1 + \sum_{\alpha=1}^{5} p^{(2\alpha)} g^{2\alpha} + O(g^{12}), \tag{32a}$$

$$u_x = u_0 + \sum_{\alpha=1}^{5} u^{(2\alpha-1)} g^{2\alpha-1} + O(g^{11}), \tag{32b}$$

$$T = 1 + \sum_{\alpha=1}^{5} T^{(2\alpha)} g^{2\alpha} + O(g^{12}). \tag{32c}$$

Note that, due to the symmetry of the Poiseuille flow, p and T are even functions of g, while u_x is an odd function of g. We further set $u_0 = 0$ which is equivalent to a Galilean transformation to a reference frame moving with the fluid velocity at $y = 0$. Since the collision frequency for the hard-spheres [25, 38] is $\nu = pT^{-1/2}$, we can express it in terms of a power series in g:

$$\nu = 1 + \nu^{(2)}g^2 + \nu^{(4)}g^4 + \nu^{(6)}g^6 + \nu^{(8)}g^8 + O(g^{10}) \quad (33)$$

where the coefficients $\nu^{(i)}$ follow from the related expressions for p and T:

$$\nu^{(2)} = p^{(2)} - \frac{1}{2}T^{(2)}, \quad (34a)$$

$$\nu^{(4)} = p^{(4)} - \frac{p^{(2)}T^{(2)}}{2} + \frac{3}{8}T^{(2)^2} - \frac{T^{(4)}}{2}, \quad (34b)$$

$$\nu^{(6)} = p^{(6)} - \frac{p^{(4)}T^{(2)}}{2} + \frac{3p^{(2)}T^{(2)^2}}{8} - \frac{5T^{(2)^3}}{16} - \frac{p^{(2)}T^{(4)}}{2} + \frac{3T^{(2)}T^{(4)}}{4} - \frac{T^{(6)}}{2}, \quad (34c)$$

$$\nu^{(8)} = p^{(8)} - \frac{p^{(6)}T^{(2)}}{2} + \frac{3p^{(4)}T^{(2)^2}}{8} - \frac{5p^{(2)}T^{(2)^3}}{16} + \frac{35T^{(2)^4}}{128} - \frac{p^{(4)}T^{(4)}}{2} + \frac{3p^{(2)}T^{(2)}T^{(4)}}{4} - \frac{15T^{(2)^2}T^{(4)}}{16} + \frac{3T^{(4)^2}}{8} - \frac{p^{(2)}T^{(6)}}{2} + \frac{3T^{(2)}T^{(6)}}{4} - \frac{T^{(8)}}{2}. \quad (34d)$$

In order to solve Eq. (29) at each order $O(g^\alpha)$, the following consistency conditions must be satisfied:

$$\left.\begin{array}{ll} \int d\boldsymbol{C} f_M \Phi = 0, & \int d\boldsymbol{C} C_y f_M \Phi = 0, \\ \int d\boldsymbol{C} C_x f_M \Phi = 0, & \int d\boldsymbol{C} C^2 f_M \Phi = 0, \end{array}\right\} \quad (35)$$

which comes from the definition of hydrodynamic fields. Finally we adopt the methodology followed by Tij and Santos [5, 14] to obtain solution of perturbation equations at different orders in $O(g^\alpha)$: (1) guess the hydrodynamic profiles and then (2) verify the validity of assumed solutions using consistency conditions [Eq. (35)].

B. Solution procedure at odd-order in g

The equation (29) at odd order in g yields

$$(1 - \mathscr{A})\Phi^{(2\alpha-1)} = \text{functional of the unknowns } u^{(2\alpha-1)} \equiv \phi^{(2\alpha-1)}, \quad (36)$$

where $\mathscr{A}$ is the operator

$$\mathscr{A} = -c_y \frac{\partial}{\partial y}. \quad (37)$$

Note that the expression for $\phi^{(2\alpha-1)}$ depends only on velocity due to the symmetry of the problem and its space dependence occurs through $u^{(2\alpha-1)}$. In order to solve the governing equation at odd order in g [Eq. (36)], firstly, we guess the velocity profile. The formal solution to Eq. (36) is

$$\Phi^{(2\alpha-1)} = \sum_{k=0}^{\infty} \mathscr{A}^k \phi^{(2\alpha-1)} \quad (38)$$

and the functional structure of $\mathscr{A}^k\phi^{(2\alpha-1)}$ remains to be the same for any k which suggests the form of the trial function for $\Phi^{(2\alpha-1)}$. Later, the precise form of $\Phi^{(2\alpha-1)}$ is obtained by inserting its trial form into Eq. (36) and verifying the consistency conditions [Eq. (35)]. Once the expression for $\Phi^{(2\alpha-1)}$ is known explicitly, the associated hydrodynamic fields and fluxes at odd orders can be determined.

C. Solution procedure at even-order in g

The equation (29) at even order in g yields

$$(1 - \mathscr{A})\Phi^{(2\alpha)} = \text{functional of unknowns } p^{(2\alpha)} \,\&\, T^{(2\alpha)} \equiv \phi^{(2\alpha)}. \quad (39)$$

At this order, the expression for $\phi^{(2\alpha)}$ depends on pressure p and temperature T as these are even functions of g and its space dependence occurs through two unknown functions $p^{(2\alpha)}$ and $T^{(2\alpha)}$. In order to solve Eq. (39), we follow the same solution procedure: (i) guess the pressure and temperature profiles, and (ii) then the form of trial function for $\Phi^{(2\alpha)}$ is to be assumed. With these assumptions, the explicit expression for $\Phi^{(2\alpha)}$ is obtained from which one can determine the associated hydrodynamic fields and fluxes at even orders.

D. First-order solution $O(g)$

To illustrate the solution procedure at odd-orders as discussed in Sec. III B, we consider Eq. (29) at first order in g:

$$(1 - \mathscr{A})\Phi^{(1)} = -2c_x\left(1 + c_y\frac{\partial u^{(1)}}{\partial y}\right) \equiv \phi^{(1)}. \quad (40)$$

The function $\phi^{(1)}$ has a known velocity dependence and its space dependence occurs through an unknown function $u^{(1)}$, representing the first-order velocity profile, which is assumed to be of parabolic shape:

$$u^{(1)}(y) = u_2^{(1)}y^2; \quad (41)$$

the quadratic-dependence of velocity in Eq. (41) follows from the well-known Navier-Stokes solution for Poiseuille flow which serves as the leading solution for velocity profile. Noting further that (i) the formal solution to Eq. (40) is $\Phi^{(1)} = \sum_{k=0}^{\infty} \mathscr{A}^k\phi^{(1)}$ and (ii) the functional

structure of $\mathscr{A}^k\phi^{(1)}$ remains the same for any k, the solution $\Phi^{(1)}$ must have the following structure,

$$\Phi^{(1)}(y,\boldsymbol{c}) = c_x\,(a_0 \,+\, a_1\,c_y^2 \,+\, a_2\,c_y\,y), \tag{42}$$

where a_0, a_1 and a_2 are unknown coefficients which must be obtained by insertion of Eq. (42) into Eq. (40). The explicit values of these coefficients are found to be

$$a_0 = -2, \quad a_1 = 4\,u_2^{(1)} \quad \text{and} \quad a_2 = -4\,u_2^{(1)}. \tag{43}$$

Now substituting Eq. (42) into the third consistency condition of Eq. (35), we find $u_2^{(1)} = 1$, and the remaining three consistency conditions of Eq. (35) are satisfied via symmetry. Therefore, the explicit form of $\Phi^{(1)}$ is

$$\Phi^{(1)}(y,\boldsymbol{c}) = 2\,c_x(2c_y^2 - \,2c_y y - \,1). \tag{44}$$

With the aid of Eq. (44), we can determine the fluxes (Eqs. (12) and (13)) at first order in g. The "non-zero" components of fluxes at $O(g)$ are given by

$$P_{yx}^{(1)}(y) = -2\,y, \quad q_x^{(1)}(y) = 1. \tag{45}$$

E. Second-order solution $O(g^2)$

At second order in g, Eq. (29) yields

$$\begin{aligned}(1-\mathscr{A})\Phi^{(2)} = &\left[\frac{\partial}{\partial c_x} - 2c_x\left(1 + c_y\frac{\partial u^{(1)}}{\partial y}\right)\right]\Phi^{(1)}\\ &-c_y\left[\frac{\partial p^{(2)}}{\partial y} + \left(c^2 - \frac{5}{2}\right)\frac{\partial T^{(2)}}{\partial y}\right]\\ &+2u^{(1)}\left(1 + c_y\frac{\partial u^{(1)}}{\partial y}\right) \equiv \phi^{(2)}.\end{aligned} \tag{46}$$

It is clear that $\phi^{(2)}$ has a known dependence on pressure and temperature gradients but its spatial-dependence occurs through $p^{(2)}$ and $T^{(2)}$. Following the solution procedure of Sec. III C, we guess the second-order pressure and temperature profiles as:

$$p^{(2)}(y) = p_2^{(2)}y^2 \quad \text{and} \quad T^{(2)}(y) = T_2^{(2)}y^2 + T_4^{(2)}y^4. \tag{47}$$

Since the solution to Eq. (46) is $\Phi^{(2)} = \sum_{k=0}^{\infty}\mathscr{A}^k\phi^{(2)}$, the structure of $\mathscr{A}^k\phi^{(2)}$ suggests a trial function of the form

$$\begin{aligned}\Phi^{(2)}(y,\boldsymbol{c}) = &\,b_0 + b_1c_y^2 + b_2c_y y + b_3y^2 + b_4c_y^4 + b_5c_y^3y\\ &+b_6c_y^2y^2 + b_7c_y y^3 + c_x^2\big(b_8 + b_9c_y^2 + b_{10}c_y y\\ &+b_{11}y^2 + b_{12}c_y^4 + b_{13}c_y^3y + b_{14}c_y^2y^2\big)\\ &+c^2\big(b_{15} + b_{16}c_y^2 + b_{17}c_y y + b_{18}y^2 + b_{19}c_y^4\\ &+b_{20}c_y^3y + b_{21}c_y^2y^2 + b_{22}c_y y^3\big).\end{aligned} \tag{48}$$

Insertion of Eq. (48) into Eq. (46) allows one to obtain the coefficients b_i's in terms of $p_2^{(2)}, T_2^{(2)}$, and $T_4^{(2)}$ (not shown). Here, the third consistency condition of Eq. (35) is satisfied via symmetry, while the second consistency condition of Eq. (35) holds identically, irrespective of the values of $p_2^{(2)}, T_2^{(2)}$, and $T_4^{(2)}$; the remaining consistency conditions of Eq. (35) result in

$$p_2^{(2)} = \frac{24}{5}, \quad T_2^{(2)} = \frac{76}{25}, \quad T_4^{(2)} = -\frac{4}{15}. \tag{49}$$

The explicit expressions for the coefficients b_i's are therefore found, leading to the following expression for $\Phi^{(2)}$:

$$\begin{aligned}\Phi^{(2)}(y,\boldsymbol{c}) = -\frac{2}{75}[&240c_y^6 - 240c_y^5y - 75(-1 + 2c_x^2 + y^2)\\ &-8c_y^3y(9 + 30c_z^2 - 195c_x^2 + 5y^2)\\ &+24c_y^4(3 + 10c_z^2 - 65c_x^2 + 5y^2)\\ &-2c_y y\{5(-9 + 5y^2) + 2c_z^2(-57 + 10y^2)\\ &+2c_x^2(93 + 10y^2)\} + 6c_y^2\{5(-8 + 5y^2)\\ &-16c_x^2(-7 + 5y^2) + c_z^2(-38 + 20y^2)\}].\end{aligned} \tag{50}$$

Using Eq. (50), the second-order contributions to the flux fields (Eqs. (12) and (13)) are determined:

$$P_{xx}^{(2)}(y) = \frac{656}{25} + \frac{56}{5}y^2,\ P_{yy}^{(2)} = -\frac{612}{25},\ q_y^{(2)}(y) = \frac{4}{3}y^3. \tag{51}$$

Note that other flux terms at second-order [$P_{xy}^{(2)}$ and $q_x^{(2)}$] are zero.

F. Third to tenth order solutions, $O(g^\alpha, \alpha = 3,\ldots,10)$

The explicit expressions for $\Phi^{(\alpha\geq 3)}$ at third- and higher-orders are too lengthy and cumbersome to be written here, but are relegated to the Supplemental Material I [29]. The related expressions for hydrodynamic [$u_x^{(\alpha\geq 3)}$, $T^{(\alpha\geq 3)}$ and $p^{(\alpha\geq 3)}$] and flux fields [$P_{ij}^{(\alpha\geq 3)}$, $q_x^{(\alpha\geq 3)}$ and $q_y^{(\alpha\geq 3)}$] are given in Sec. A.9 of Supplemental Material II [29]).

G. Putting all together: solutions for hydrodynamic fields

Here we present the main results on hydrodynamic profiles obtained from the perturbation expansion. By retaining terms up-to tenth-order in the (dimensionless) gravitational acceleration, the expressions for the velocity, temperature and pressure can be written compactly as

$$\begin{aligned}u_x(y) = u_0 + \left(\frac{\rho_0 g}{2\eta_0}\right)y^2 + u_2^{(3)}\left(\frac{m^3\eta_0 g^3}{4\rho_0 T_0^3}\right)y^2\\ +u_4^{(3)}\left(\frac{m^2\rho_0 g^3}{8\eta_0 T_0^2}\right)y^4 + \cdots + O(g^{11}),\end{aligned} \tag{52}$$

$$T(y)=T_0\Bigg[1+T_4^{(2)}\left(\frac{m\rho_0^2g^2}{8\eta_0^2T_0}\right)y^4+T_2^{(2)}\left(\frac{mg}{2T_0}\right)^2y^2 +T_2^{(4)}\left(\frac{m^5\eta_0^2g^4}{8\rho_0^2T_0^5}\right)y^2+\cdots\Bigg]+O(g^{12}), \tag{53}$$

$$p(y)=p_0\Bigg[1+p_2^{(2)}\left(\frac{mg}{2T_0}\right)^2y^2+p_2^{(4)}\left(\frac{m^5\eta_0^2g^4}{8\rho_0^2T_0^5}\right)y^2 +p_4^{(4)}\left(\frac{mg}{2T_0}\right)^4y^4+\cdots\Bigg]+O(g^{12}), \tag{54}$$

with their exact-forms being given in Eqs. (A.48), (A.49) and (A.50), respectively, of Sec. A.9 in Supplemental Material II [29]]. The coefficients $p_i^{(\alpha)}, u_i^{(\alpha)}$ and $T_i^{(\alpha)}$ can be found in Secs. III.D and III.E and Secs A.1 to A.8 of Supplemental Material II. In the following section we compare the above solutions for hard-spheres with previous results of Tij and Santos [5] for Maxwell molecules.

H. Comparison of results between hard spheres and Maxwell molecules

Tij and Santos [5] analysed the acceleration-driven Poiseuille flow for Maxwell molecules and determined perturbation solution up to sixth-order in g^*. In particular, they analysed this problem in terms of a dimensionless space variable s defined as

$$s(y)=\frac{1}{c_0}\int_0^y\nu(y')dy'. \tag{55}$$

The above relation can be inverted to yield an expression for dimensionless transverse coordinate (employed in the present analysis)

$$y^*(s)=\int_0^s\frac{ds'}{\nu^*(s')}\equiv\frac{y\nu_0}{c_0}. \tag{56}$$

Since $\nu^*=p^*/T^*$ for Maxwell molecules and we substitute $p^*(=1+p^{(2)}g^{*^2}+\cdots)$ and $T^*(=1+T^{(2)}g^{*^2}+\cdots)$, into Eq. (55); after integration, we get a relation between s and y^*.

$$s=y^*+g^{*^2}y^{*^3}\left(\frac{11}{75}+\frac{1}{150}y^{*^2}\right)+\cdots. \tag{57}$$

Substituting Eq. (57) into Eqs. (45)-(47) of Ref. [5] and converting the resulted expressions into real units, we obtain the hydrodynamic fields:

$$u_x(y)=\underline{u_0+\left(\frac{\rho_0g}{2\eta_0}\right)y^2}+\frac{2737}{25}\left(\frac{m^3\eta_0g^3}{\rho_0T_0^3}\right)y^2 +\frac{76}{75}\left(\frac{m^2\rho_0g^3}{\eta_0T_0^2}\right)y^4+\frac{1}{150}\left(\frac{m\rho_0^3g^3}{\eta_0^3T_0}\right)y^6 +O(g^5), \tag{58}$$

$$T(y)=\underline{T_0\Bigg[1-\frac{1}{30}\left(\frac{m\rho_0^2g^2}{\eta_0^2T_0}\right)y^4+\frac{76}{25}\left(\frac{mg}{2T_0}\right)^2y^2} -\frac{203783296}{3125}\left(\frac{m^5\eta_0^2g^4}{8\rho_0^2T_0^5}\right)y^2-\frac{439864}{625}\left(\frac{mg}{2T_0}\right)^4y^4 -\frac{32656}{5625}\left(\frac{m^3\rho_0^2g^4}{32\eta_0^2T_0^3}\right)y^6-\frac{64}{1125}\left(\frac{m^2\rho_0^4g^4}{64\eta_0^4T_0^2}\right)y^8\Bigg] +O(g^6), \tag{59}$$

$$p(y)=\underline{p_0\Bigg[1+\frac{6}{5}\left(\frac{mg}{T_0}\right)^2y^2}-\frac{2612976}{125}\left(\frac{m^5\eta_0^2g^4}{8\rho_0^2T_0^5}\right)y^2 -\frac{17136}{125}\left(\frac{mg}{2T_0}\right)^4y^4+\frac{64}{125}\left(\frac{m^3\rho_0^2g^4}{32\eta_0^2T_0^3}\right)y^6\Bigg] +O(g^6). \tag{60}$$

that hold for Maxwell molecules. Note that the underlined terms in above equations are of second-order $O(g^2)$.

To compare Eqs. (58)-(60) with present hard sphere results, first we substitute the coefficients $p_i^{(j)}, u_i^{(j)}$ and $T_i^{(j)}$ [given in Secs. III.D, III.E and Supplemental Material II (Sec. A)] in Eqs. (52)-(54) to obtain

$$u_x(y)=\underline{u_0+\left(\frac{\rho_0g}{2\eta_0}\right)y^2}+\frac{2726}{25}\left(\frac{m^3\eta_0g^3}{\rho_0T_0^3}\right)y^2 +\frac{43}{40}\left(\frac{m^2\rho_0g^3}{\eta_0T_0^2}\right)y^4+\frac{7}{1800}\left(\frac{m\rho_0^3g^3}{\eta_0^3T_0}\right)y^6 +O(g^5), \tag{61}$$

$$T(y)=\underline{T_0\Bigg[1-\frac{1}{30}\left(\frac{m\rho_0^2g^2}{\eta_0^2T_0}\right)y^4+\frac{76}{25}\left(\frac{mg}{2T_0}\right)^2y^2} -\frac{199914896}{3125}\left(\frac{m^5\eta_0^2g^4}{8\rho_0^2T_0^5}\right)y^2-\frac{1287016}{1875}\left(\frac{mg}{2T_0}\right)^4y^4 -\frac{34768}{5625}\left(\frac{m^3\rho_0^2g^4}{32\eta_0^2T_0^3}\right)y^6-\frac{248}{7875}\left(\frac{m^2\rho_0^4g^4}{64\eta_0^4T_0^2}\right)y^8\Bigg]+ +O(g^6), \tag{62}$$

$$p(y)=\underline{p_0\Bigg[1+\frac{6}{5}\left(\frac{mg}{T_0}\right)^2y^2}-\frac{2523696}{125}\left(\frac{m^5\eta_0^2g^4}{8\rho_0^2T_0^5}\right)y^2 -\frac{15008}{125}\left(\frac{mg}{2T_0}\right)^4y^4+\frac{64}{125}\left(\frac{m^3\rho_0^2g^4}{32\eta_0^2T_0^3}\right)y^6\Bigg] +O(g^6). \tag{63}$$

It is clear that the above solutions [Eqs. (61)-(63)] for hard spheres are identical with the corresponding solutions [Eqs. (58)-(60)] for Maxwell molecules up-to second-order in g (the underlined terms). This finding also holds for the components of pressure tensor and heat flux as verified later. Therefore we conclude that the present series solutions for hard spheres differ from those for Maxwell molecules [5] beyond second-order $O(g^2)$.

IV. HYDRODYNAMICS: TEMPERATURE PROFILE AND ITS BIMODAL SHAPE

In this section, we discuss the unique characteristics of the temperature profile in Poiseuille flow based on the present higher-order solution. To analyze the characteristics of temperature profile, Eq. (53), we scale the y-coordinate in terms of the centreline mean free-path,

$$\lambda_0 = \frac{1}{\sqrt{2}\pi n_0 \sigma^2}, \tag{64}$$

which is the average distance traveled by a particle between two successive collisions at the channel center ($y = 0$). In terms of the centreline thermal velocity (c_0) and the collision frequency (ν_0, Eq. (19)), λ_0 can be expressed as

$$\lambda_0 = \frac{8}{5\sqrt{\pi}} \frac{c_0}{\nu_0}. \tag{65}$$

Now we introduce a dimensionless number, namely, the Froude number $\mathrm{Fr} = g\lambda/c^2$, which is defined as the square of the ratio between the gravitational (external) and thermal velocity scales: it measures the influence of gravity on the flow field. The Froude number at the channel centreline is given by

$$\mathrm{Fr}_0 = \frac{g\lambda_0}{c_0^2} \equiv \frac{8}{5\sqrt{\pi}} g^*, \tag{66}$$

which is proportional to g^* defined in Eq. (28).

A. Rarefaction effects on temperature

In terms of the centreline mean-free path (λ_0) and Froude number (Fr_0), the temperature profile, Eq. (53), becomes

$$\frac{T(y)}{T_0} = 1 + T^{(\mathrm{II})} + T^{(\mathrm{IV})} + T^{(\mathrm{VI})} + T^{(\mathrm{VIII})} + T^{(\mathrm{X})} + O(\mathrm{Fr}_0^{12}), \tag{67}$$

where

$$\begin{aligned} T^{(\mathrm{II})} &= \mathrm{Fr}_0^2 \left[A_T^{(2)} + A_T^{(4)} \left(\tfrac{y}{\lambda_0}\right)^2 \right] \left(\tfrac{y}{\lambda_0}\right)^2, \\ T^{(\mathrm{IV})} &= \mathrm{Fr}_0^4 \textstyle\sum_{\alpha=1}^{4} B_T^{(2\alpha)} \left(\tfrac{y}{\lambda_0}\right)^{2\alpha}, \\ T^{(\mathrm{VI})} &= \mathrm{Fr}_0^6 \textstyle\sum_{\alpha=1}^{6} C_T^{(2\alpha)} \left(\tfrac{y}{\lambda_0}\right)^{2\alpha}, \\ T^{(\mathrm{VIII})} &= \mathrm{Fr}_0^8 \textstyle\sum_{\alpha=1}^{8} D_T^{(2\alpha)} \left(\tfrac{y}{\lambda_0}\right)^{2\alpha}, \\ T^{(\mathrm{X})} &= \mathrm{Fr}_0^{10} \textstyle\sum_{\alpha=1}^{10} E_T^{(2\alpha)} \left(\tfrac{y}{\lambda_0}\right)^{2\alpha}, \end{aligned} \tag{68}$$

and the expressions for coefficients $(A_T^{(\alpha)}, \ldots, E_T^{(\alpha)})$ are provided in Sec. B.2 of Supplemental Material II [29].

Figures 2(a) and 2(b) display the temperature profiles $T(y)$ [solution of Eq. (67)] for $\mathrm{Fr}_0 = 10^{-4}$ and $\mathrm{Fr}_0 = 10^{-3}$, respectively; in each panel the dimensionless temperature $T(y)/T_0$ is plotted against y/λ_0, where λ_0 is the centreline mean-free path defined in Eq. (64). It is clear that the temperature profile $T(y)$ has a local minimum at the channel centreline (i.e. at $y = 0$) which is surrounded by two maxima on either side of it at the some distance of few mean-free paths from the channel centreline. Such bimodal-shape of the temperature profile is a unique characteristic feature of the rarefaction of the gas undergoing Poiseuille flow [5, 16]. Further, it can be observed that the variations between different orders solutions of temperature profiles are negligible for the case of $\mathrm{Fr}_0 = 10^{-4}$ (Fig. 2a), but the deviations are noticeable at higher values of Froude numbers (Fig. 2b).

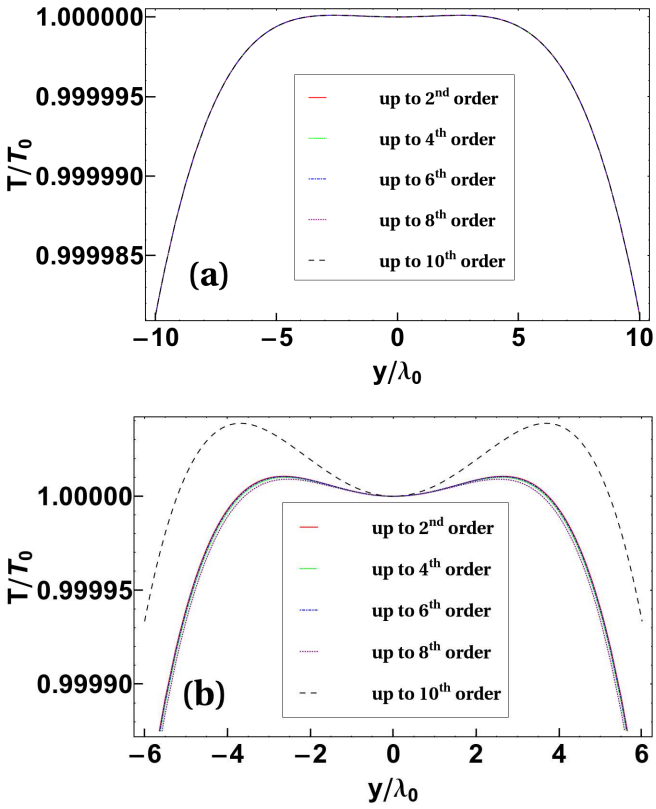

FIG. 2. Temperature profiles for (a) $\mathrm{Fr}_0 = 10^{-4}$ and (b) $\mathrm{Fr}_0 = 10^{-3}$. The red solid, green tiny dashed, blue dot-dashed, purple dotted and black large dashed lines represent the 2nd order, 4th order, 6th order, 8th order and 10th order series solutions, respectively. Note that different order solutions are indistinguishable in panel *a*, while the 10th order solution is clearly separated from the (almost indistinguishable) lower-order solutions in panel *b*.

Retaining only the second-order terms $[O(\mathrm{Fr}_0^2)]$ in the temperature profile, its first few derivatives can be evaluated as

$$\begin{aligned} \mathrm{Fr}_0^{-2} \tfrac{\mathrm{d}T}{\mathrm{d}\tilde{y}} &= 2A_T^{(2)}\tilde{y} + 4A_T^{(4)}\tilde{y}^3 \\ \mathrm{Fr}_0^{-2} \tfrac{\mathrm{d}^2T}{\mathrm{d}\tilde{y}^2} &= 2A_T^{(2)} + 12A_T^{(4)}\tilde{y}^2 \\ \mathrm{Fr}_0^{-2} \tfrac{\mathrm{d}^4T}{\mathrm{d}\tilde{y}^4} &= 24A_T^{(4)} \end{aligned} \tag{69}$$

where $\tilde{y} = y/\lambda_0$ is the normalized transverse coordinate.

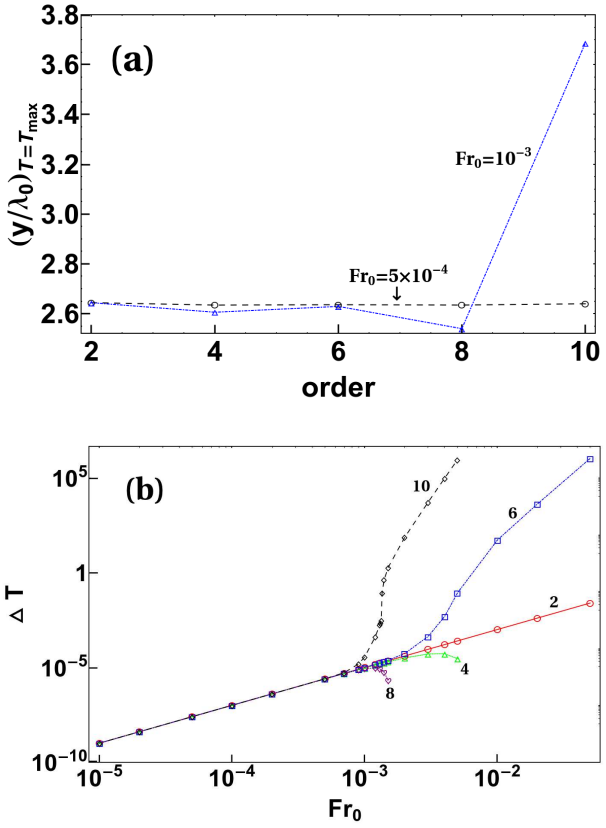

FIG. 3. (a) Variations of the location of the maximum temperature, $(y/\lambda_0)_{T=T_{\max}}$, with order of approximation. (b) Variations of $\Delta T(= T_{\max}/T_0 - 1)$ with Fr_0. The red solid, green tiny dashed, blue dot-dashed, purple dotted and black large dashed lines represent the 2$^{\text{nd}}$ order, 4$^{\text{th}}$ order, 6$^{\text{th}}$ order, 8$^{\text{th}}$ order and 10$^{\text{th}}$ order series solutions, respectively.

Since $A_T^{(2)} = 76/25$ and $A_T^{(4)} = -256/375\pi$, we have

$$\left(\frac{\mathrm{d}T}{\mathrm{d}\tilde{y}}\right)_{y=0} = 0, \left(\frac{\mathrm{d}^2T}{\mathrm{d}\tilde{y}^2}\right)_{y=0} > 0 \text{ and } \left(\frac{\mathrm{d}^4T}{\mathrm{d}\tilde{y}^4}\right)_{y=0} < 0, \tag{70}$$

which corresponds to a local minimum of temperature at the channel centreline ($y = 0$). In rarefied Poiseuille flow, the maximum temperature occurs in the bulk away from the channel centreline and the location of this maximum can be obtained by setting $dT/dy = 0$, yielding

$$\left(\frac{y}{\lambda_0}\right)_{T=T_{\max}} = \pm\sqrt{-\frac{A_T^{(2)}}{2A_T^{(4)}}} = \pm\frac{\sqrt{285\pi}}{8\sqrt{2}} \approx \pm 2.64. \tag{71}$$

Therefore, at leading order $O(\mathrm{Fr}_0^2)$, the temperature maximum is located at about 2.6 mean free-paths away from the channel centreline. It is clear from above equation that $y(T = T_{\max}) = 0$ when $A_T^{(2)} = 0$, and hence the origin of the centreline temperature-minimum is tied to the quadratic term $[A_T^{(2)} \neq 0]$ in the temperature profile. This finding also agrees with the perturbation solution of the Navier-Stokes-order hydrodynamic equations, Eq. (17), for Poiseuille flow [14]:

$$\frac{T_{NS}(y)}{T_0} = 1 - \left(\frac{m\rho_0^2 g^2}{10\eta_0^2 T_0}\right) y^4 + O(\mathrm{Fr}_0^4). \tag{72}$$

Note from Eq. (71) that the transverse location of the temperature maximum is independent of the forcing parameter (Fr_0); the explicit dependence on the Froude number appears when the higher-order terms are incorporated to the temperature profile. For example, for the fourth-order $O(\mathrm{Fr}_0^4)$ temperature profile, an approximate solution of $dT/dy = 0$ yields a modified expression for Eq. (71):

$$\left(\frac{y}{\lambda_0}\right)_{T=T_{\max}} \approx \pm\sqrt{-\frac{A_T^{(2)} + \mathrm{Fr}_0^2 B_T^{(2)}}{2\left(A_T^{(4)} + \mathrm{Fr}_0^2 B_T^{(4)}\right)}}, \tag{73}$$

and at tenth-order $O(\mathrm{Fr}_0^{10})$

$$\left(\frac{y}{\lambda_0}\right)_{T=T_{\max}} \approx \pm\sqrt{-\frac{A_T^{(2)} + \mathrm{Fr}_0^2 B_T^{(2)} + \mathrm{Fr}_0^4 C_T^{(2)} + \mathrm{Fr}_0^6 D_T^{(2)} + \mathrm{Fr}_0^8 E_T^{(2)}}{2\left(A_T^{(4)} + \mathrm{Fr}_0^2 B_T^{(4)} + \mathrm{Fr}_0^4 C_T^{(4)} + \mathrm{Fr}_0^6 D_T^{(4)} + \mathrm{Fr}_0^8 E_T^{(4)}\right)}}. \tag{74}$$

It is clear from Sec. B.2 of Supplemental Material II [29] that the signs of $A_T^{(2)}$ (positive), $B_T^{(2)}$ (negative), $C_T^{(2)}$ (positive), $D_T^{(2)}$ (negative) and $E_T^{(2)}$ (positive) and those of $A_T^{(4)}$ (negative), $B_T^{(4)}$ (positive), $C_T^{(4)}$ (negative), $D_T^{(4)}$ (positive) and $E_T^{(4)}$ (negative) alternate between positive and negative values. The oscillatory nature of $(y/\lambda_0)_{T=T_{\max}}$ is also evident in Fig. 3(a) with increasing order of approximation.

To quantify the bimodal shape of the temperature profile (such as in Fig. 2), we introduce a quantity $\triangle T = (T_{\max} - T_0)/T_0$, defined as the relative difference between the maximum and minimum of temperature – this is dubbed *excess temperature* [19, 20] which is a measure of the degree of the bimodality of the temperature profile. The Navier-Stokes model predicts a zero value

for $\triangle T$, whereas the present solution predicts non-zero values for the same as it is evident from Fig. 3(b); at second-order $O(\mathrm{Fr}_0^2)$ an exact expression for excess temperature is found:

$$\frac{\triangle T}{\mathrm{Fr}_0^2} = -\frac{{A_T^{(2)}}^2}{4A_T^{(4)}} + O(\mathrm{Fr}_0^2). \tag{75}$$

In Fig. 3(b) the excess temperature shows oscillating behaviour with increasing order of terms in the temperature profile as it is evident from a comparison between 4th-order and 6th-order solution for $\triangle T$. Such oscillatory series solution (with the perturbation parameter) as depicted in Fig. 3(a,b) is a clear signal of the asymptotic/divergent nature of the underlying power series – this issue will be further discussed in the context of rheological quantities in Secs. V and VI.

It should be noted that the DSMC (direct simulation Monte Carlo) simulations [16, 20] of gravity-driven Poiseuille flow of a molecular gas suggest that the temperature bimodality $\triangle T$ should increase monotonically with increasing gravitational strength (Fr_0) as well as with increasing Knudsen number. Therefore, the leading-order solution for $\triangle T$ in Fig. 3(b) correctly captures the trend of DSMC results, along with 6th and 10th order solutions. On the other hand, the 4th- and 8th-order solutions in Fig. 3(b) suggest a decreasing trend of $\triangle T$ with increasing Fr_0 beyond some critical value of Fr_0.

B. Relation between Fr_0 and Kn

In most DSMC simulations of Poiseuille flows [8, 16, 20, 21], the gravitational acceleration is set fixed to a small value, and the Knudsen number is varied by varying either the number density or the channel width. In fact, there is a one-to-one relation between the local Froude number [Eq. (66)] and the Knudsen number via the following relation

$$\mathrm{Fr}_0 = \widehat{g}\ \mathrm{Kn}_0 \left(\frac{T_w}{T_0}\right) \equiv \widehat{g}\ \mathrm{Kn} \left(\frac{T_w}{T_0}\right)\left(\frac{n_{\mathrm{av}}}{n_0}\right), \tag{76}$$

where $\mathrm{Kn}_0 = \lambda_0/W$ is the centreline Knudsen number and W is the width of channel (see Fig. 1). The dimensionless parameter $\widehat{g}$ is defined via

$$\widehat{g} = \frac{gW}{\frac{2k_B T_w}{m}}, \tag{77}$$

where T_w is the wall-temperature (which can be fixed at 1 for thermal-walls [20]); Kn is the "global" Knudsen number

$$\mathrm{Kn} = \frac{\lambda}{W} = \frac{1}{\sqrt{2}\pi n_{\mathrm{av}}\sigma^2 W}, \tag{78}$$

based on the equilibrium mean-free path of the gas at the mean density $n = n_{\mathrm{av}}$. Note that the dimensionless acceleration $\widehat{g}$ in Eq. (77) is a measure of the strength of the body force acting on a particle travelling a distance W (between two walls); this parameter $\widehat{g}$ is routinely specified in particle-based simulations of Poiseuille flow [8, 12, 16, 20].

In present paper, all results are presented as functions of the centreline Froude number Fr_0. Equation (76) implies that the conclusions drawn from the present analysis are likely to carry over to the corresponding variations with the Knudsen number Kn as long as the dimensionless acceleration $\widehat{g}$ [Eq. (77)] is small enough such that the perturbation expansion holds.

V. RHEOLOGY AND HEAT FLUX

A. Pressure tensor and normal stress differences

The power-series expressions for the non-zero components of the pressure tensor P_{ij} up to tenth-order in Fr_0, expressed in real units, can be rewritten in terms of the centreline mean-free path (λ_0) and Froude number (Fr_0). For example, the streamwise component (P_{xx}) of pressure can be expressed as

$$\frac{P_{xx}}{p_0} = 1 + P_{xx}^{(\mathrm{II})} + P_{xx}^{(\mathrm{IV})} + P_{xx}^{(\mathrm{VI})} + P_{xx}^{(\mathrm{VIII})} + P_{xx}^{(\mathrm{X})} + O(\mathrm{Fr}_0^{12}), \tag{79}$$

where

$$\begin{aligned}
P_{xx}^{(\mathrm{II})} &= \mathrm{Fr}_0^2 \left[A_{P_{xx}}^{(0)} + A_{P_{xx}}^{(2)} \left(\tfrac{y}{\lambda_0}\right)^2\right], \\
P_{xx}^{(\mathrm{IV})} &= \mathrm{Fr}_0^4 \textstyle\sum_{\alpha=0}^{3} B_{P_{xx}}^{(2\alpha)} \left(\tfrac{y}{\lambda_0}\right)^{2\alpha}, \\
P_{xx}^{(\mathrm{VI})} &= \mathrm{Fr}_0^6 \textstyle\sum_{\alpha=0}^{5} C_{P_{xx}}^{(2\alpha)} \left(\tfrac{y}{\lambda_0}\right)^{2\alpha}, \\
P_{xx}^{(\mathrm{VIII})} &= \mathrm{Fr}_0^8 \textstyle\sum_{\alpha=0}^{7} D_{P_{xx}}^{(2\alpha)} \left(\tfrac{y}{\lambda_0}\right)^{2\alpha}, \\
P_{xx}^{(\mathrm{X})} &= \mathrm{Fr}_0^{10} \textstyle\sum_{\alpha=0}^{9} E_{P_{xx}}^{(2\alpha)} \left(\tfrac{y}{\lambda_0}\right)^{2\alpha},
\end{aligned} \tag{80}$$

and the expressions for the coefficients $(A_{P_{xx}}^{(\alpha)}, \ldots, E_{P_{xx}}^{(\alpha)})$ are provided in Sec. B.3 of Supplemental Material II [29]. The normal component (P_{yy}) of pressure tensor can be expressed as

$$\frac{P_{yy}}{p_0} = 1 + P_{yy}^{(\mathrm{II})} + P_{yy}^{(\mathrm{IV})} + P_{yy}^{(\mathrm{VI})} + P_{yy}^{(\mathrm{VIII})} + P_{yy}^{(\mathrm{X})} + O(\mathrm{Fr}_0^{12}), \tag{81}$$

where

$$\begin{aligned}
P_{yy}^{(\mathrm{II})} &= \mathrm{Fr}_0^2\ A_{P_{yy}}^{(0)}, \quad P_{yy}^{(\mathrm{IV})} = \mathrm{Fr}_0^4\ B_{P_{yy}}^{(0)} \\
P_{yy}^{(\mathrm{VI})} &= \mathrm{Fr}_0^6\ C_{P_{yy}}^{(0)}, \quad P_{yy}^{(\mathrm{VIII})} = \mathrm{Fr}_0^8\ D_{P_{yy}}^{(0)} \\
P_{yy}^{(\mathrm{X})} &= \mathrm{Fr}_0^{10}\ E_{P_{yy}}^{(0)},
\end{aligned} \tag{82}$$

with

$$A^{(0)}_{P_{yy}} = -\frac{153\pi}{16}, \quad B^{(0)}_{P_{yy}} = \frac{9152979\pi^2}{160},$$
$$C^{(0)}_{P_{yy}} = -\frac{850121653854657\pi^3}{102400},$$
$$D^{(0)}_{P_{yy}} = \frac{13756464847792449369773 1\pi^4}{16384000},$$
$$E^{(0)}_{P_{yy}} = -\frac{937606576466175266052495646216 53\pi^5}{2621440000}. \tag{83}$$

The constancy of $(A^{(0)}_{P_{yy}}, \ldots, E^{(0)}_{P_{yy}})$ follows from the y-momentum equation ($dP_{yy}/dy = 0$). The expression for P_{zz} can be obtained from

$$P_{zz} = 3p - P_{xx} - P_{yy}, \tag{84}$$

where the pressure $p(y)$ is given by [Eq. 54]

$$\frac{p(y)}{p_0} = 1 + p^{(\mathrm{II})} + p^{(\mathrm{IV})} + p^{(\mathrm{VI})} + p^{(\mathrm{VIII})} + p^{(\mathrm{X})} + O(\mathrm{Fr}_0^{12}), \tag{85}$$

with

$$p^{(\mathrm{II})} = \mathrm{Fr}_0^2 A_p^{(2)} \left(\tfrac{y}{\lambda_0}\right)^2,$$
$$p^{(\mathrm{IV})} = \mathrm{Fr}_0^4 \textstyle\sum_{\alpha=1}^{3} B_p^{(2\alpha)} \left(\tfrac{y}{\lambda_0}\right)^{2\alpha},$$
$$p^{(\mathrm{VI})} = \mathrm{Fr}_0^6 \textstyle\sum_{\alpha=1}^{5} C_p^{(2\alpha)} \left(\tfrac{y}{\lambda_0}\right)^{2\alpha},$$
$$p^{(\mathrm{VIII})} = \mathrm{Fr}_0^8 \textstyle\sum_{\alpha=1}^{7} D_p^{(2\alpha)} \left(\tfrac{y}{\lambda_0}\right)^{2\alpha},$$
$$p^{(\mathrm{X})} = \mathrm{Fr}_0^{10} \textstyle\sum_{\alpha=1}^{9} E_p^{(2\alpha)} \left(\tfrac{y}{\lambda_0}\right)^{2\alpha}. \tag{86}$$

The expressions for the coefficients $(A_p^{(\alpha)}, \ldots, E_p^{(\alpha)})$ are provided in Sec. B.3 of Supplemental Material II [29]. Transverse profiles of pressure $p(y)$, Eq. (85), has a minimum at the channel centreline ($y = 0$) whose origin is tied to the corresponding variation of its streamwise component P_{xx} (not shown).

It is clear from Eqs. (79,81,84) that the diagonal components of the pressure tensor are unequal ($P_{xx} \neq P_{yy} \neq P_{zz}$), resulting in "non-zero" normal stress differences, which are one signature of a rarefied gas. The first and second normal stress differences are defined via: $\mathcal{N}_1(y) = (P_{xx} - P_{yy})/p$ and $\mathcal{N}_2(y) = (P_{yy} - P_{zz})/p$, and employing Eq. (84) we can rewrite normal stress differences as

$$\mathcal{N}_1(y) = \frac{P_{xx} - P_{yy}}{p} \quad \text{and} \quad \mathcal{N}_2(y) = \frac{P_{xx} + 2P_{yy}}{p} - 3, \tag{87}$$

which are functions of the transverse coordinate y in the Poiseuille flow. In the remainder of this section, we analyse two normal stress differences and present some numerical results.

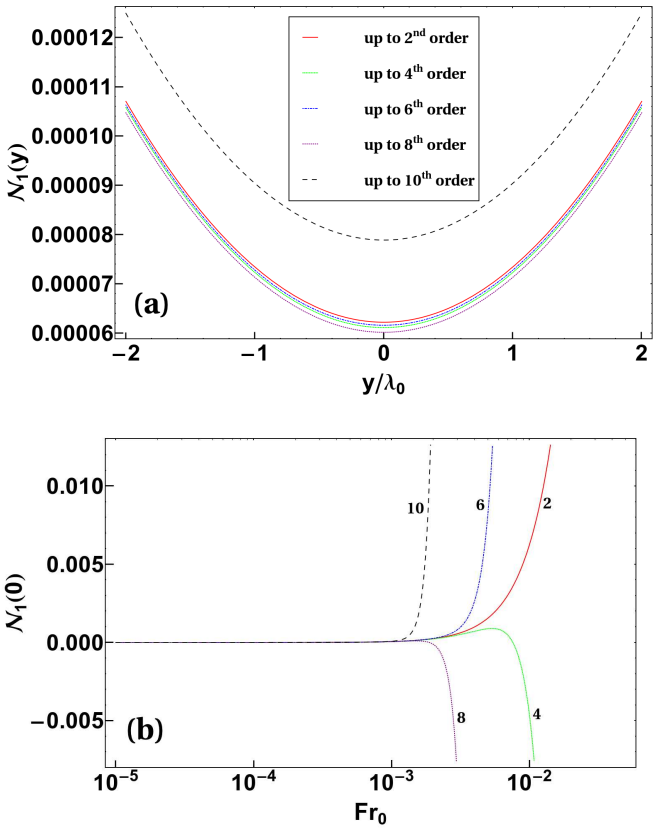

FIG. 4. (a) First normal-stress difference profiles $\mathcal{N}_1(y)$ for $\mathrm{Fr}_0 = 10^{-3}$ and (b) the variations of $\mathcal{N}_1(0)$ with Fr_0. In both panels, the red solid, green tiny dashed, blue dot-dashed, purple dotted and black large dashed lines represnt 2nd order, 4th order, 6th order, 8th order and 10th order series solutions, respectively. In panel a, except 10th-order solution, the remaining solutions are closely spaced and hence not distinguishable.

Figure 4(a) shows the transverse profiles of first normal stress difference for $\mathrm{Fr}_0 = 10^{-3}$. It is seen that the first normal stress difference remains positive in the bulk region of the channel: it is minimum at $y = 0$ and increases as one moves away from the channel centreline. Figure 4(b) displays the variation of the first normal stress difference evaluated at the channel centreline ($y = 0$) with Froude number Fr_0. From Figs. 4(a,b), we find that for Froude number less than 10^{-3}, the differences among the solutions of all orders are negligible. However, it is evident from Fig. 4(b) that the solutions at second, sixth and tenth order in g diverge upward whereas the solutions at fourth and eighth order in g diverge downward for Fr_0 greater than 10^{-3}. Such oscillatory nature of partial sums of an infinite series is indicative of the divergent character of the underlying series for $\mathcal{N}_1$. The latter issue

can be understood by analysing the expression for $\mathcal{N}_1(0)$:

$$\mathcal{N}_1(0) = \mathrm{Fr}_0^2 \left[\left(A^{(0)}_{P_{xx}} - A^{(0)}_{P_{yy}} \right) + \left(B^{(0)}_{P_{xx}} - B^{(0)}_{P_{yy}} \right) \mathrm{Fr}_0^2 + \left(C^{(0)}_{P_{xx}} - C^{(0)}_{P_{yy}} \right) \mathrm{Fr}_0^4 + \left(D^{(0)}_{P_{xx}} - D^{(0)}_{P_{yy}} \right) \mathrm{Fr}_0^6 + \left(E^{(0)}_{P_{xx}} - E^{(0)}_{P_{yy}} \right) \mathrm{Fr}_0^8 \right]. \quad (88)$$

From Eq. (80) and Eq. (B.6) [in Sec. B.3 of Supplemental Material II [29]], it is easy to verify that

$$A^{(0)}_{P_{xx}} - A^{(0)}_{P_{yy}} = \tfrac{11\pi}{16}, \quad B^{(0)}_{P_{xx}} - B^{(0)}_{P_{yy}} = -\tfrac{17488781\pi^2}{160}, \quad C^{(0)}_{P_{xx}} - C^{(0)}_{P_{yy}} > 0, \quad D^{(0)}_{P_{xx}} - D^{(0)}_{P_{yy}} < 0, \quad E^{(0)}_{P_{xx}} - E^{(0)}_{P_{yy}} > 0, \quad (89)$$

and hence the coefficients of the power-series, Eq. (88), alternate in sign with increasing order of Fr_0^2. This implies that the truncated sum of Eq. (88) would show oscillatory behaviour with increasing Fr_0, indicating a possible divergent or asymptotic character of the full series – this will be further analysed in Sec. VI via Padé approximation method.

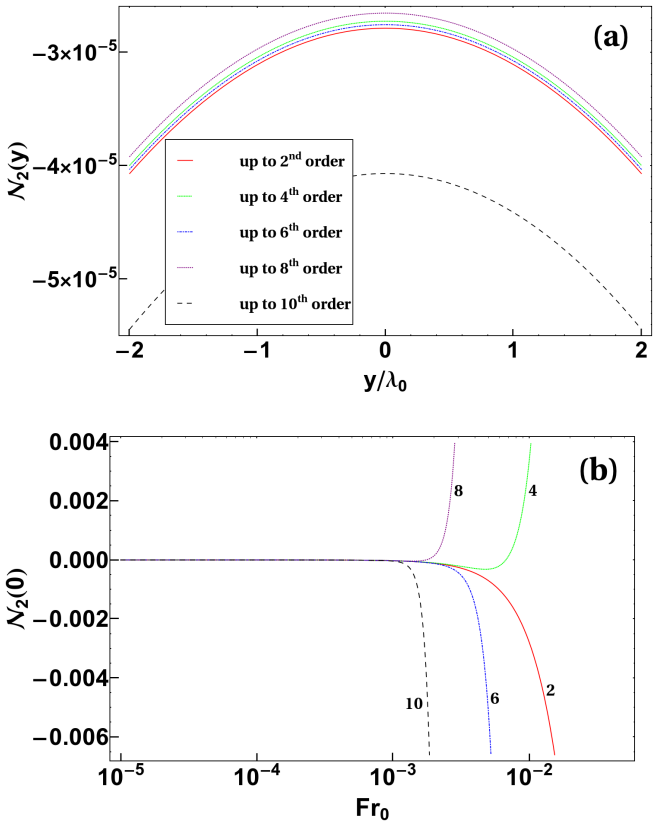

FIG. 5. (a) Second normal-stress difference profiles $\mathcal{N}_2(y)$ for $\mathrm{Fr}_0 = 10^{-3}$, and (b) the variations of $\mathcal{N}_2(0)$ with Fr_0. In both panels (a) and (b), the red solid, green tiny dashed, blue dot-dashed, purple dotted and black large dashed lines represent the 2nd order, 4th order, 6th order, 8th order and 10th order series solutions, respectively.

The second normal stress difference profiles at $\mathrm{Fr}_0 = 10^{-3}$ are presented in Fig. 5(a) which shows that $\mathcal{N}_2(y)$ approaches its maximum at $y = 0$ and decreases away from the channel centreline. Figure 5(b) shows the variations of the second normal stress difference evaluated at the channel centreline ($y = 0$),

$$\mathcal{N}_2(0) = \mathrm{Fr}_0^2 \left[\left(A^{(0)}_{P_{xx}} + 2A^{(0)}_{P_{yy}} \right) + \left(B^{(0)}_{P_{xx}} + 2B^{(0)}_{P_{yy}} \right) \mathrm{Fr}_0^2 + \left(C^{(0)}_{P_{xx}} + 2C^{(0)}_{P_{yy}} \right) \mathrm{Fr}_0^4 + \left(D^{(0)}_{P_{xx}} + 2D^{(0)}_{P_{yy}} \right) \mathrm{Fr}_0^6 + \left(E^{(0)}_{P_{xx}} + 2E^{(0)}_{P_{yy}} \right) \mathrm{Fr}_0^8 \right], \quad (90)$$

against Froude number. It is seen in Fig. 5(b) that the solutions from second, sixth and tenth order in Fr_0 show downward divergence whereas the fourth and eighth order solutions show upward divergence for $\mathrm{Fr}_0 > 10^{-3}$ which is opposite as compared to the related behaviour of $\mathcal{N}_1$ [see Fig. 4(b)]. The coefficients in the above power-series satisfy

$$A^{(0)}_{P_{xx}} + 2A^{(0)}_{P_{yy}} = -\tfrac{71\pi}{8}, \quad B^{(0)}_{P_{xx}} + 2B^{(0)}_{P_{yy}} = \tfrac{4985078\pi^2}{80}, \quad C^{(0)}_{P_{xx}} + 2C^{(0)}_{P_{yy}} < 0, \; D^{(0)}_{P_{xx}} + 2D^{(0)}_{P_{yy}} > 0, \quad E^{(0)}_{P_{xx}} + 2E^{(0)}_{P_{yy}} < 0, \quad (91)$$

indicating oscillatory behaviour of Eq. (90) with increasing order of terms in Fr_0 as confirmed in Fig. 5(b).

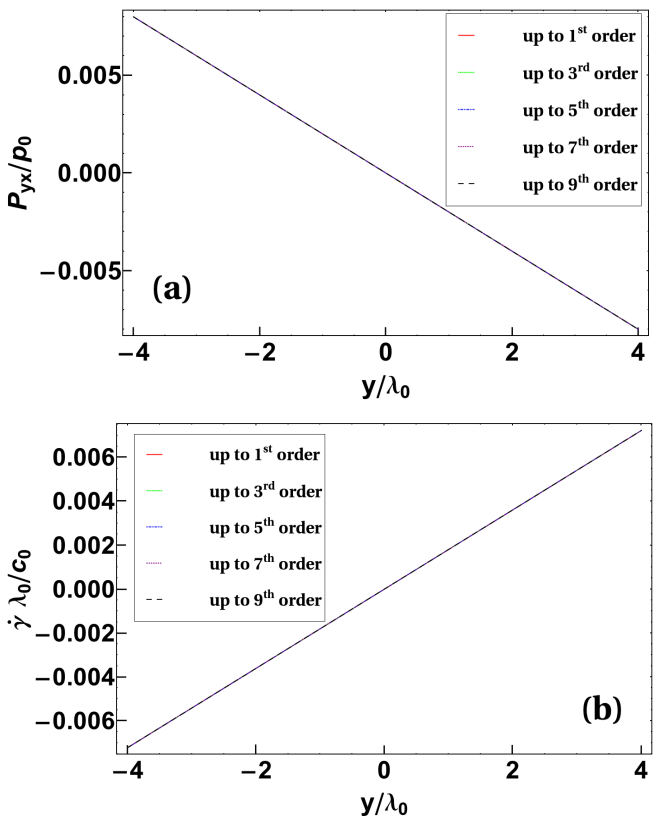

FIG. 6. Profiles of (a) the shear stress (P_{yx}) and (b) the shear rate ($\dot{\gamma} = \frac{du_x}{dy}$) for $\mathrm{Fr}_0 = 10^{-3}$. Note that different order solutions are indistinguishable in both panels.

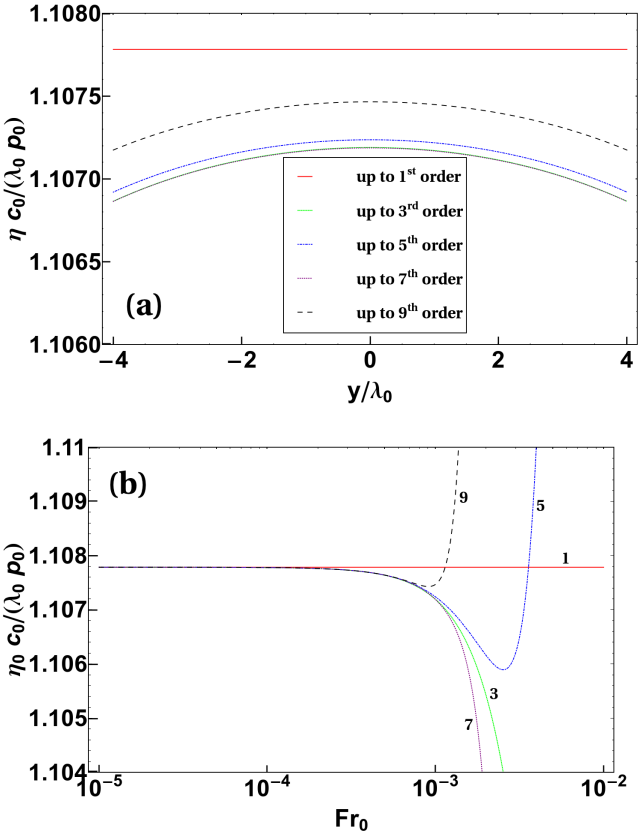

FIG. 7. (a) Transverse profiles of the shear viscosity [$\eta(y) = -P_{yx}/\frac{du_x}{dy}$] for $\mathrm{Fr}_0 = 10^{-3}$. (b) Shear viscosity evaluated at $y = 0$ versus Froude number Fr_0.

B. Shear stress and viscosity

The expression for the shear stress P_{yx} can be written as

$$\frac{P_{yx}}{p_0} = P_{yx}^{(\mathrm{I})} + P_{yx}^{(\mathrm{III})} + P_{yx}^{(\mathrm{V})} + P_{yx}^{(\mathrm{VII})} + P_{yx}^{(\mathrm{IX})} + O(\mathrm{Fr}_0^{11}), \tag{92}$$

where

$$\begin{aligned} P_{yx}^{(\mathrm{I})} &= \mathrm{Fr}_0 A_{P_{yx}}^{(1)}\left(\tfrac{y}{\lambda_0}\right), \\ P_{yx}^{(\mathrm{III})} &= \mathrm{Fr}_0^3 \textstyle\sum_{\alpha=1}^{2} B_{P_{yx}}^{(2\alpha+1)}\left(\tfrac{y}{\lambda_0}\right)^{2\alpha+1}, \\ P_{yx}^{(\mathrm{V})} &= \mathrm{Fr}_0^5 \textstyle\sum_{\alpha=1}^{4} C_{P_{yx}}^{(2\alpha+1)}\left(\tfrac{y}{\lambda_0}\right)^{2\alpha+1}, \\ P_{yx}^{(\mathrm{VII})} &= \mathrm{Fr}_0^7 \textstyle\sum_{\alpha=1}^{6} D_{P_{yx}}^{(2\alpha+1)}\left(\tfrac{y}{\lambda_0}\right)^{2\alpha+1}, \\ P_{yx}^{(\mathrm{IX})} &= \mathrm{Fr}_0^9 \textstyle\sum_{\alpha=1}^{8} E_{P_{yx}}^{(2\alpha+1)}\left(\tfrac{y}{\lambda_0}\right)^{2\alpha+1}, \end{aligned} \tag{93}$$

and the coefficients $(A_{P_{yx}}^{(\alpha)}, \ldots, E_{P_{yx}}^{(\alpha)})$ are givens in Sec. B.3 of Supplemental Material II [29]. The transverse profiles of the shear stress at different orders of approximation are displayed in Fig. 6(a). The shear viscosity is defined via

$$\eta(y) = -\frac{P_{xy}}{\dot{\gamma}}, \tag{94}$$

and the local shear rate $\dot{\gamma}(y) = du_x/dy$ can be obtained from Eq. (52) [Eq. (B2) in Sec. B.1 of Supplemental Material II [29]], see Fig. 6(b) for the shear-rate variation across the channel centreline. Inserting Eq. (92) and Eq. (B.2-B.3) into Eq. (94), the shear viscosity has been determined. The Navier-Stokes-order viscosity can be found from the leading-order expression of the shear stress $P_{yx} \equiv P_{yx}^{(\mathrm{I})}$ and the velocity profile $u_x^{(\mathrm{I})} \equiv \mathrm{Fr}_0 A_{u_x}^{(2)}(y/\lambda_0)^2$, with $A_{u_x}^{(2)} = 8/5\sqrt{\pi}$: from Eq. (94) and using $\dot{\gamma} \equiv du^{(I)}/dy$, the dimensionless shear viscosity is found to be

$$\eta_{NS} = \frac{-A_{P_{yx}}^{(1)}}{2A_{u_x}^{(2)}} = \frac{5\sqrt{\pi}}{8} \tag{95}$$

that holds at NS-order.

Transverse profiles of the shear viscosity $\eta(y)$ [Eq. (94)] and its centreline variation $\eta_0 \equiv \eta(y=0)$ with Froude number are displayed in Figs. 7(a) and 7(b), respectively. The viscosity is maximum at the channel centreline where the shear rate is zero, and decreases away from the centreline (where the shear rate is higher, viz. Fig. 6(b)) – this is a characteristic of the shear-thinning nature of the gas undergoing Poiseuille flow. Figure 7(b) confirms the oscillatory behaviour of the shear viscosity η_0 with increasing order of approximation. The expression of viscosity at the channel centreline, $\eta_0 = \eta(0)$, is given by

$$\begin{aligned}\eta_0 &= \frac{-A_{P_{yx}}^{(1)}}{2\left(A_{u_x}^{(2)} + B_{u_x}^{(2)}\mathrm{Fr}_0^2 + C_{u_x}^{(2)}\mathrm{Fr}_0^4 + D_{u_x}^{(2)}\mathrm{Fr}_0^6 + E_{u_x}^{(2)}\mathrm{Fr}_0^8\right)} \\ &= \frac{1}{A_{u_x}^{(2)} + B_{u_x}^{(2)}\mathrm{Fr}_0^2 + C_{u_x}^{(2)}\mathrm{Fr}_0^4 + D_{u_x}^{(2)}\mathrm{Fr}_0^6 + E_{u_x}^{(2)}\mathrm{Fr}_0^8}.\end{aligned} \tag{96}$$

From Eq. (B.3) in Sec B.1 of Supplemental Material II [29], we note that $A_{u_x}^{(2)} = 8/5\sqrt{\pi} > 0$, $B_{u_x}^{(2)} > 0$, $C_{u_x}^{(2)} < 0$, $D_{u_x}^{(2)} > 0$ and $E_{u_x}^{(2)} < 0$ (that alternate in signs), confirming the oscillatory nature of η_0 in Fig. 7(b).

C. Tangential and normal heat flux

The tangential or streamwise component of heat flux (q_x) can be rewritten in terms of the centreline mean-free path (λ_0) and Froude number (Fr_0) as

$$\begin{aligned}\frac{q_x}{p_0 c_0} &= q_x^{(\mathrm{I})} + q_x^{(\mathrm{III})} + q_x^{(\mathrm{V})} + q_x^{(\mathrm{VII})} \\ &\quad + q_x^{(\mathrm{IX})} + O(\mathrm{Fr}_0^{11}),\end{aligned} \tag{97}$$

where

$$\begin{aligned}q_x^{(\mathrm{I})} &= \mathrm{Fr}_0 A_{q_x}^{(0)}, \\ q_x^{(\mathrm{III})} &= \mathrm{Fr}_0^3 \textstyle\sum_{\alpha=1}^{3} B_{q_x}^{(2\alpha-2)} \left(\frac{y}{\lambda_0}\right)^{2(\alpha-1)}, \\ q_x^{(\mathrm{V})} &= \mathrm{Fr}_0^5 \textstyle\sum_{\alpha=1}^{5} C_{q_x}^{(2\alpha-2)} \left(\frac{y}{\lambda_0}\right)^{2(\alpha-1)}, \\ q_x^{(\mathrm{VII})} &= \mathrm{Fr}_0^7 \textstyle\sum_{\alpha=1}^{7} D_{q_x}^{(2\alpha-2)} \left(\frac{y}{\lambda_0}\right)^{2(\alpha-1)}, \\ q_x^{(\mathrm{IX})} &= \mathrm{Fr}_0^9 \textstyle\sum_{\alpha=1}^{9} E_{q_x}^{(2\alpha-2)} \left(\frac{y}{\lambda_0}\right)^{2(\alpha-1)}.\end{aligned} \tag{98}$$

The expression for the normal component of heat flux (q_y) is

$$\begin{aligned}\frac{q_y}{p_0 c_0} &= q_y^{(\mathrm{II})} + q_y^{(\mathrm{IV})} + q_y^{(\mathrm{VI})} + q_y^{(\mathrm{VIII})} \\ &\quad + q_y^{(\mathrm{X})} + O(\mathrm{Fr}_0^{12}),\end{aligned} \tag{99}$$

where

$$\begin{aligned}q_y^{(\mathrm{II})} &= \mathrm{Fr}_0^2 A_{q_y}^{(3)} \left(\frac{y}{\lambda_0}\right)^3, \\ q_y^{(\mathrm{IV})} &= \mathrm{Fr}_0^4 \textstyle\sum_{\alpha=1}^{3} B_{q_y}^{(2\alpha+1)} \left(\frac{y}{\lambda_0}\right)^{2\alpha+1}, \\ q_y^{(\mathrm{VI})} &= \mathrm{Fr}_0^6 \textstyle\sum_{\alpha=1}^{5} C_{q_y}^{(2\alpha+1)} \left(\frac{y}{\lambda_0}\right)^{2\alpha+1}, \\ q_y^{(\mathrm{VIII})} &= \mathrm{Fr}_0^8 \textstyle\sum_{\alpha=1}^{7} D_{q_y}^{(2\alpha+1)} \left(\frac{y}{\lambda_0}\right)^{2\alpha+1}, \\ q_y^{(\mathrm{X})} &= \mathrm{Fr}_0^{10} \textstyle\sum_{\alpha=1}^{9} E_{q_y}^{(2\alpha+1)} \left(\frac{y}{\lambda_0}\right)^{2\alpha+1}.\end{aligned} \tag{100}$$

The expressions for the coefficients $(A_{q_x}^{(\alpha)}, \ldots, E_{q_x}^{(\alpha)})$ and $(A_{q_y}^{(\alpha)}, \ldots, E_{q_y}^{(\alpha)})$ are provided in Sec. B.4 of Supplemental Material II [29].

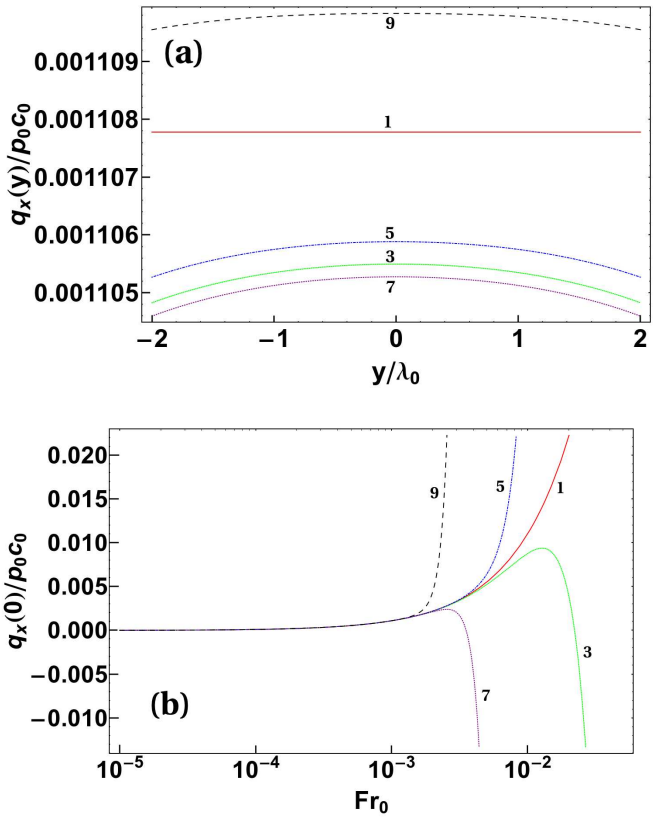

FIG. 8. Profiles of dimensionless (a) x-component of heat flux ($q_x^* = q_x/p_0c_0$) for $\mathrm{Fr}_0 = 10^{-3}$ and (b) x-component of heat flux ($q_x^* = q_x/p_0c_0$) evaluated at channel centreline ($y = 0$), with Fr_0. In all panels, the red solid, green tiny dashed, blue dot-dashed, purple dotted and black large dashed lines represents the solutions of respective orders.

The profiles of the tangential heat-flux at $\mathrm{Fr}_0 = 10^{-3}$ are shown in Fig. 8(a). Note that according to Navier-Stokes model, the tangential component of heat flux (q_x)

is zero, but it is non-zero according to the kinetic theory description [5, 28]. Further from Fig. 8(a), while the first-order solution for tangential heat flux predicts a constant value across the channel width, the higher-order solutions have a maximum at $y = 0$. The positive values of q_x imply that the tangential heat flux is directed along a direction opposing the flow (see Fig. 1). Figure 8(b) displays tangential heat flux evaluated at the channel centreline ($y = 0$),

$$q_x(0) = \mathrm{Fr}_0 \left[A_{q_x}^{(0)} + B_{q_x}^{(0)} \mathrm{Fr}_0^2 + C_{q_x}^{(0)} \mathrm{Fr}_0^4 + D_{q_x}^{(0)} \mathrm{Fr}_0^6 + E_{q_x}^{(0)} \mathrm{Fr}_0^8 \right], \tag{101}$$

against the Froude number. Clearly, the higher-order solutions show oscillating behaviour at $\mathrm{Fr}_0 > 10^{-3}$, and $q_x(0)$ can become negative (see 3rd and 7th order solutions), indicating $q_x(0)$ being directed along the flow-direction. The oscillatory nature of this series, Eq. (101), can be tied to the fact that its coefficients

$$A_{q_x}^{(0)} = \tfrac{5\sqrt{\pi}}{8} > 0,\ B_{q_x}^{(0)} = -\tfrac{105045\pi^{3/2}}{256} < 0,\ C_{q_x}^{(0)} > 0,\quad D_{q_x}^{(0)} < 0,\quad E_{q_x}^{(0)} > 0, \tag{102}$$

alternate in signs with increasing order in Fr_0.

The profiles of the normal component of heat flux $q_y(y)$ are presented in Fig. 9(a) for $\mathrm{Fr}_0 = 10^{-3}$; the differences among the solutions of different orders in Fr_0 are almost negligible. The shape of q_y-profile can be understood from the corresponding profile of the temperature gradient shown in Fig. 9(b). The positivity of thermal conductivity [$\propto -q_y/(dT/dy)$, Fourier's law] would require that q_y and dT/dy are of opposite signs– this condition is satisfied only at $|y| > y_{\max}$ (i.e. the locations at which $T = T_{\max}$). Within the central core $-y_{\max} \le y < y_{\max}$ of the channel, the heat still flows outwards from the colder channel centre to the hotter region – this departure from Fourier's law can be reconciled when we incorporate the added effects of viscous heating [$P_{yx}(du_x/dy)$] in the energy balance equation.

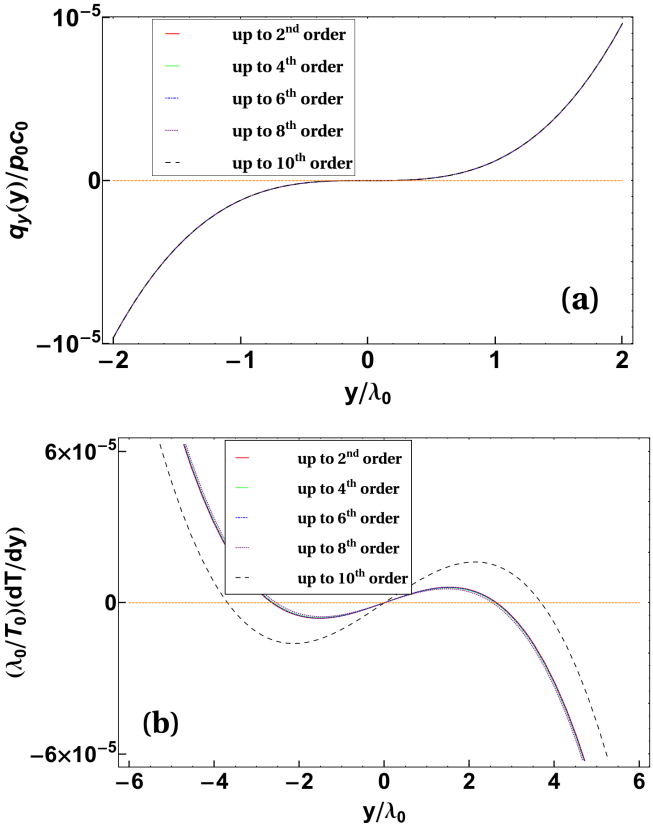

FIG. 9. Profiles of (a) dimensionless normal heat flux ($q_y^* = q_y/p_0c_0$) and (b) temperature gradient (dT/dy) for $\mathrm{Fr}_0 = 10^{-3}$. In panel b, the zero-crossings of dT/dy at $y = \pm y_{\max}$ correspond to the locations of termperature-maxima $T = T_{\max}$ (see Fig. 2). In all panels, the red solid, green tiny dashed, blue dot-dashed, purple dotted and black large dashed lines represents the solutions of respective orders.

1. *Thermal conductivity*

Considering leading-order expressions for q_y [Eq. (99)] and the temperature gradient dT/dy [Eq. (69)], an expression for thermal conductivity can be derived:

$$\begin{aligned} \kappa_{yy}(y) &= -\frac{q_y}{(dT/dy)} \\ &\equiv \left(-\frac{A_{q_y}^{(3)}}{4A_T^{(4)}} \right) \left[1 - \frac{A_T^{(2)}}{2A_T^{(4)}} \left(\frac{y}{\lambda_0} \right)^{-2} + \cdots \right] \\ &= \kappa_{NS} \left[1 + \left(\frac{y_{\max}}{y} \right)^2 + \cdots \right] \end{aligned} \tag{103}$$

where $y_{\max}$ is the transverse location of temperature-maximum [see Eq. (71)] and

$$\kappa_{NS} = -\frac{A_{q_y}^{(3)}}{4A_T^{(4)}} = \frac{25\sqrt{\pi}}{32} \tag{104}$$

is the dimensionless thermal conductivity at the Navier-Stokes order, which remains constant, expectedly, across

the channel since $y_{\max} \propto A_T^{(2)} \to 0$ at this order. Furthermore, at NS-order, $q_y \propto g^2 y^3$ and $T(y) = T_0 - (\cdot) g^2 y^4$ and hence the expression in Eq. (104) also follows from $\kappa = -q_y/(dT/dy)$.

For the present unidirectional rarefied Poiseuille flow, the thermal conductivity is characterized by a rank-2 tensor

$$\begin{pmatrix} q_x \\ q_y \end{pmatrix} = - \begin{bmatrix} \kappa_{xx} & \kappa_{xy} \\ \kappa_{yx} & \kappa_{yy} \end{bmatrix} \begin{pmatrix} \frac{dT}{dx} \\ \frac{dT}{dy} \end{pmatrix}. \tag{105}$$

where κ_{yy} is given by Eq. (103). Using this, an expression for the cross thermal conductivity κ_{xy} can be obtained from Eq. (97):

$$\begin{aligned} \kappa_{xy} &= -\frac{q_x}{(dT/dy)} \\ &\approx \frac{-A_{q_x}^{(0)}}{4A_T^{(4)}\mathrm{Fr}_0} \left[1 + \left(\frac{y_{\max}}{y} \right)^2 + \cdots \right] \left(\frac{\lambda_0}{y} \right)^3 . \end{aligned} \tag{106}$$

Since $A_{q_x}^{(0)} > 0$ and $A_T^{(4)} < 0$, the positivity of κ_{xy} is guaranteed; note that Eq. (106) makes sense only when $q_x \neq 0$ which results from the shearing/rarefaction effects.

VI. CONVERGENCE ISSUES AND PADÉ APPROXIMATION

A. Convergence issues with series solutions

It is clear from the results presented in Secs. IV and V that the perturbation series solutions for (i) the temperature $T(y)$ [Fig. 2(b)], (ii) the first normal stress difference $\mathcal{N}_1(y)$ [Fig. 4(a)], (iii) the second normal-stress difference $\mathcal{N}_2(y)$ [Fig. 5(a)], (iv) the shear viscosity $\eta(y)$ [Fig. 7(a)] and (v) the tangential heat flux $q_x(y)$ [Fig. 8(a)] do not converge when the higher-order terms in each series are sequentially added. Moreover, the rheological fields evaluated at the channel centreline show oscillating behaviour with increasing higher-order terms in each series as confirmed in Figs. 4(b), 5(b), 7(b) and 8(b), indicating that the underlying series solutions could be divergent. For example, recall from Eq. (88), that the coefficients in the series solution for first normal stress difference $\mathcal{N}_1(0)$ alternate in signs with increasing order of the perturbation parameter (the Froude number Fr_0). Similar characteristic features are well-known for the Chapman-Enskog-type perturbation solutions of the Boltzmann equation in the context of both molecular and granular gases [30–33].

To check the region of convergence of the adopted series expansion for the present problem of gravity-driven Poiseuille flow, we apply convergence acceleration method to the current series solutions. In particular, we have used Padé approximation [34] method to the present problem. A brief account of the Padé approximation method is given in the next section, followed by its application to the present problem.

B. Padé approximation

The objective of approximation/summation theory is to represent a given function by a convergent expression, which is the limit of a convergent series and the limit of convergent integral in Euler and Borel summation methods, respectively. The main drawback of the summation methods (such as Euler and Borel summation) is that all terms in a power series representation of a function must be known which is not possible in almost all realistic perturbation problems. Therefore, a method is needed which only requires a finite number of terms of a divergent series as input. Padé approximation [34] is a well-known summation method having a key property: *extracting the information from the power series expansion with only a few known terms*, introduced by Padé in 1892. The main idea of this method is to replace a power series representation of a function by a sequence of rational functions [35–37], i.e., a Padé approximant of a function is the ratio of two polynomials which are constructed from the coefficients of the Taylor series expansion of the given function.

For a given power series $\sum_{\alpha=0}^{\infty} a_\alpha x^\alpha$, the Padé approximation is defined as [35–37]

$$\mathcal{P}_M^N(x) = \frac{\mathcal{A}_M(x)}{\mathcal{B}_N(x)} \equiv \mathcal{P}[M,N] \approx \sum_{\alpha=0}^{\infty} a_\alpha x^\alpha, \tag{107}$$

where

$$\mathcal{A}_M(x) = \sum_{\alpha=0}^{M} \mathcal{A}_\alpha x^\alpha, \quad \mathcal{B}_N(x) = \sum_{\alpha=0}^{N} \mathcal{B}_\alpha x^\alpha, \tag{108}$$

and we choose $\mathcal{B}_0 = 1$ without loss of generality. There are $M+1$ independent numerator coefficients $(\mathcal{A}_0, \ldots, \mathcal{A}_M)$ and N independent denominator coefficients $(\mathcal{B}_1, \ldots, \mathcal{B}_N)$, a total $(M+N+1)$ unknown coefficients in Eq. (107). Therefore, the Padé approximation of the power series can be written as

$$\sum_{\alpha=0}^{\infty} a_\alpha x^\alpha = \frac{\sum_{\alpha=0}^{M} \mathcal{A}_\alpha x^\alpha}{1 + \sum_{\alpha=1}^{N} \mathcal{B}_\alpha x^\alpha} + O(x^{M+N+1}). \tag{109}$$

To determine $(M+N+1)$ unknown coefficients, the first $(M+N+1)$ terms of the power series $\sum_{\alpha=0}^{\infty} a_\alpha x^\alpha$ are compared with the respective terms in the Taylor series expansion of $\mathcal{P}_M^N(x)$. The emerging rational function $\mathcal{P}[M,N] \equiv \mathcal{P}_M^N(x)$, given by Eq. (109), is called a Padé approximant to the given power series; if $M = N$, then $\mathcal{P}[M,M]$ is called a "diagonal" Padé approximant.

It is clear from Eq. (109) that one needs to know only the first $(M+N+1)$ terms in the power series representation of a function to construct its Padé approximant $\mathcal{P}[M,N]$, and it involves only algebraic operations. Due to this reason, the Padé summation is more convenient for computational purposes than the Borel summation

method, which requires one to integrate the analytic continuation of a function defined by a power series over an infinite range. For the sake of illustration, here we determine Padé approximant of the Maclaurin series expansion of $\tan^{-1} x$,

$$\tan^{-1} x = \int \frac{dx}{1+x^2} \approx x - \frac{x^3}{3} + \frac{x^5}{5} - \frac{x^7}{7} + \frac{x^9}{9}, \quad (110)$$

by retaining terms up to ninth-order. Note that the radius of convergence of Maclaurin series is 1, although $\tan^{-1} x$ is defined for all x.

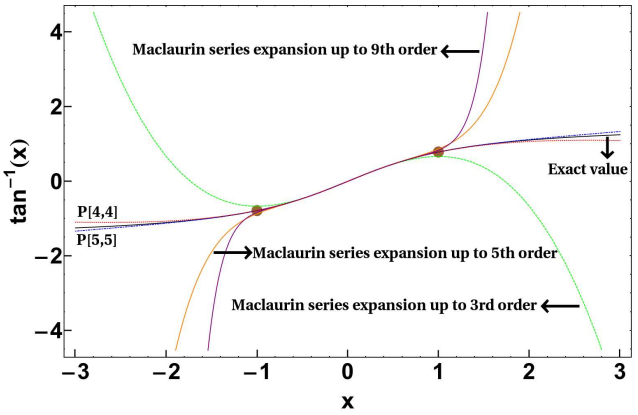

FIG. 10. Diagonal Padé approximants $\mathcal{P}[4,4]$ and $\mathcal{P}[5,5]$ versus Maclaurin series expansion for $\tan^{-1} x$. Filled circles at $x = \pm 1$ represent two singularities of the Maclaurin series whose radius of convergence is 1.

The Padé summation $\mathcal{P}[5,5]$ of Eq. (110) is given by

$$x - \frac{x^3}{3} + \frac{x^5}{5} - \frac{x^7}{7} + \frac{x^9}{9} = \frac{\sum_{\alpha=0}^{5} \mathcal{A}_\alpha x^\alpha}{1 + \sum_{\alpha=1}^{5} \mathcal{B}_\alpha x^\alpha} + O(x^{11}). \quad (111)$$

By equating the coefficients of x^n on both sides, the unknown coefficients of $\mathcal{P}[5,5]$ are found to be

$$\begin{aligned} &\mathcal{A}_0 = 0 = \mathcal{A}_2 = \mathcal{A}_4,\ \mathcal{A}_1 = 1,\ \mathcal{A}_3 = \tfrac{7}{9},\ \mathcal{A}_5 = \tfrac{64}{945}, \\ &\mathcal{B}_1 = 0 = \mathcal{B}_3 = \mathcal{B}_5,\ \mathcal{B}_2 = \tfrac{10}{9},\quad \mathcal{B}_4 = \tfrac{5}{21}. \end{aligned} \quad (112)$$

Therefore, the diagonal Padé approximations $\mathcal{P}[4,4]$ and $\mathcal{P}[5,5]$ of Eq. (110) are given by

$$\mathcal{P}_4^4[\tan^{-1} x] = \frac{x + \frac{11x^3}{21}}{1 + \frac{6x^2}{7} + \frac{3x^4}{35}}, \quad (113a)$$

$$\mathcal{P}_5^5[\tan^{-1} x] = \frac{x + \frac{7}{9}x^3 + \frac{64}{945}x^5}{1 + \frac{10}{9}x^2 + \frac{5}{21}x^4}. \quad (113b)$$

Figure 10 shows the convergence of diagonal Padé approximants $\mathcal{P}[5,5]$ and $\mathcal{P}[4,4]$ in comparison to Maclaurin series expansion (3rd, 5th and 9th order) for $\tan^{-1} x$. It is evident from this figure that the higher-order Maclaurin series solutions diverge as one moves away from $x = 0$, whereas the diagonal Padé approximants still approximate the exact value of $\tan^{-1}(x)$ accurately. In fact, due to the singularity of the Maclaurin series at $x = \pm 1$ (marked by filled circles in Fig. 10), the higher-order series solution is useless at $|x| \geq 1$. On the other hand, it is seen in Fig. 10 that increasing the order of the diagonal Padé approximant leads to more accurate (converged) solution to the exact value of $\tan^{-1} x$ at $|x| > 1$.

C. Application of Padé approximation to present problem

Here we use Padé approximation to assess the convergence of series expressions for $\mathcal{N}_1(0)$, $\mathcal{N}_2(0)$, $\eta(0)$ and $q_x(0)$, with each quantity being evaluated at the centreline of the channel. For the power-series expression of $\mathcal{N}_1(0)$ in Eq. (88), we have determined its first three diagonal Padé approximants $\mathcal{P}_3^3$, $\mathcal{P}_5^5$ and $\mathcal{P}_7^7$:

$$\begin{aligned} \mathcal{N}_1^{[3,3]}(0) &\equiv \mathcal{P}_3^3\left[\mathcal{N}_1(0)\right] = \tfrac{19.81\pi \mathrm{Fr}_0^2}{1+5516.96\pi \mathrm{Fr}_0^2}, \\ \mathcal{N}_1^{[5,5]}(0) &= \tfrac{19.81\pi \mathrm{Fr}_0^2 + \mathcal{C}_{\mathcal{N}_1}^{(1)} \mathrm{Fr}_0^4}{1+\mathcal{C}_{\mathcal{N}_1}^{(2)} \mathrm{Fr}_0^2 + \mathcal{C}_{\mathcal{N}_1}^{(3)} \mathrm{Fr}_0^4}, \\ \mathcal{N}_1^{[7,7]}(0) &= \tfrac{19.81\pi \mathrm{Fr}_0^2 + \mathcal{C}_{\mathcal{N}_1}^{(4)} \mathrm{Fr}_0^4 + \mathcal{C}_{\mathcal{N}_1}^{(5)} \mathrm{Fr}_0^6}{1+\mathcal{C}_{\mathcal{N}_1}^{(6)} \mathrm{Fr}_0^2 + \mathcal{C}_{\mathcal{N}_1}^{(7)} \mathrm{Fr}_0^4 + \mathcal{C}_{\mathcal{N}_1}^{(8)} \mathrm{Fr}_0^6}, \end{aligned} \quad (114)$$

where the coefficients $\mathcal{C}_{\mathcal{N}_1}^{(\alpha)}$ are

$$\begin{aligned} &\mathcal{C}_{\mathcal{N}_1}^{(1)} = 19919216.61\pi^2,\ \mathcal{C}_{\mathcal{N}_1}^{(2)} = 1010903.29\pi, \\ &\mathcal{C}_{\mathcal{N}_1}^{(3)} = 4816102120.58\pi^2,\ \mathcal{C}_{\mathcal{N}_1}^{(4)} = -2.65 \times 10^7 \pi^2, \\ &\mathcal{C}_{\mathcal{N}_1}^{(5)} = -1.10 \times 10^{14} \pi^3,\ \mathcal{C}_{\mathcal{N}_1}^{(6)} = -1.33 \times 10^6 \pi, \\ &\mathcal{C}_{\mathcal{N}_1}^{(7)} = -5.56 \times 10^{12} \pi^2,\ \mathcal{C}_{\mathcal{N}_1}^{(8)} = -2.89 \times 10^{16} \pi^3. \end{aligned} \quad (115)$$

The numerical results are displayed in Fig. 11 – while panel *a* compares $\mathcal{N}_1^{[7,7]}(0)$ with the corresponding series solutions of different orders, the panel *b* compares three Padé approximants among themselves. The positivity of the first normal stress difference is reproduced by all three Padé approximants at any value of Froude number Fr_0 – this is a crucial prediction of Padé approximants since (i) the Chapman-Enskog solution of the Boltzmann equation [26] for shear flow and (ii) the DSMC simulation of acceleration-driven Poiseuille flow [20] confirmed that $\mathcal{N}_1(0)$ must be positive [and $\mathcal{N}_2(0)$ must be negative] at any Froude/Knudsen number. The inset in Fig. 11(b) indicates that the variations among $\mathcal{P}_3^3$, $\mathcal{P}_5^5$ and $\mathcal{P}_7^7$ is less than 4% at $\mathrm{Fr}_0 = 0.01$. Note that the leading–order (i.e. the second-order in Fr_0) series solution for $\mathcal{N}_1(0)$, although positive, differs from the leading Padé approximant $\mathcal{P}_3^3\left[\mathcal{N}_1(0)\right]$ by more than 200% at $\mathrm{Fr}_0 = 0.01$; however, the related differences are negligible at a lower Froude number of $\mathrm{Fr}_0 = 0.001$. Therefore, the leading Padé approximant $\mathcal{P}_3^3\left[\mathcal{N}_1(0)\right]$ can be used for a much larger range of the Froude number.

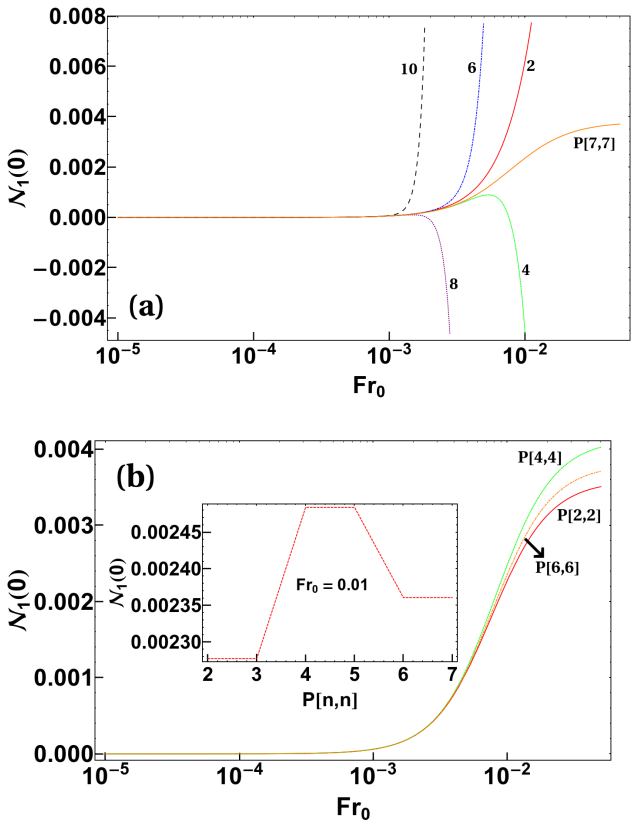

FIG. 11. First normal-stress difference evaluated at channel centreline ($y = 0$) with Froude number Fr_0: (a) different order series solutions with 7th-order Padé approximant and (b) comparison among three Padé approximants. Inset in panel b shows "diagonal" Padé approximants at $\mathrm{Fr}_0 = 0.01$.

The third-, fifth- and seventh-order diagonal Padé approximations of Eq. (90) for the second normal-stress difference $\mathcal{N}_2(0)$ are given by

$$\begin{aligned}
\mathcal{N}_2^{[3,3]}(0) &\equiv \mathcal{P}_3^3\left[\mathcal{N}_2(0)\right] = \frac{-8.87\pi\mathrm{Fr}_0^2}{1+7021.23\pi\mathrm{Fr}_0^2},\\
\mathcal{N}_2^{[5,5]}(0) &= \frac{-8.87\pi\mathrm{Fr}_0^2+\mathcal{C}_{\mathcal{N}_2}^{(1)}\mathrm{Fr}_0^4}{1+\mathcal{C}_{\mathcal{N}_1}^{(2)}\mathrm{Fr}_0^2+\mathcal{C}_{\mathcal{N}_2}^{(3)}\mathrm{Fr}_0^4},\\
\mathcal{N}_2^{[7,7]}(0) &= \frac{-8.87\pi\mathrm{Fr}_0^2+\mathcal{C}_{\mathcal{N}_2}^{(4)}\mathrm{Fr}_0^4+\mathcal{C}_{\mathcal{N}_2}^{(5)}\mathrm{Fr}_0^6}{1+\mathcal{C}_{\mathcal{N}_2}^{(6)}\mathrm{Fr}_0^2+\mathcal{C}_{\mathcal{N}_2}^{(7)}\mathrm{Fr}_0^4+\mathcal{C}_{\mathcal{N}_2}^{(8)}\mathrm{Fr}_0^6},
\end{aligned} \tag{116}$$

with

$$\begin{aligned}
&\mathcal{C}_{\mathcal{N}_2}^{(1)} = -9770495.97\pi^2,\ \mathcal{C}_{\mathcal{N}_2}^{(2)} = 1107922.19\pi,\\
&\mathcal{C}_{\mathcal{N}_2}^{(3)} = 6671573529.16\pi^2,\ \mathcal{C}_{\mathcal{N}_2}^{(4)} = 1.31\times10^{7}\pi^2,\\
&\mathcal{C}_{\mathcal{N}_2}^{(5)} = 5.79\times10^{13}\pi^3,\ \mathcal{C}_{\mathcal{N}_2}^{(6)} = -1.47\times10^{6}\pi,\\
&\mathcal{C}_{\mathcal{N}_2}^{(7)} = -6.54\times10^{12}\pi^2,\ \mathcal{C}_{\mathcal{N}_2}^{(8)} = -4.31\times10^{16}\pi^3.
\end{aligned} \tag{117}$$

The numerical results are shown in Fig. 12 – while panel a compares $\mathcal{N}_2^{[7,7]}(0)$ with the respective series solutions of different orders, the panel b compares three Padé approximants among themselves at $\mathrm{Fr}_0 = 0.01$. The negativity [20, 26] of the second normal-stress difference at any Fr_0 is captured by all three Padé approximants, and hence they are likely to be valid for a larger range of Fr_0 as in the case of the first normal-stress difference.

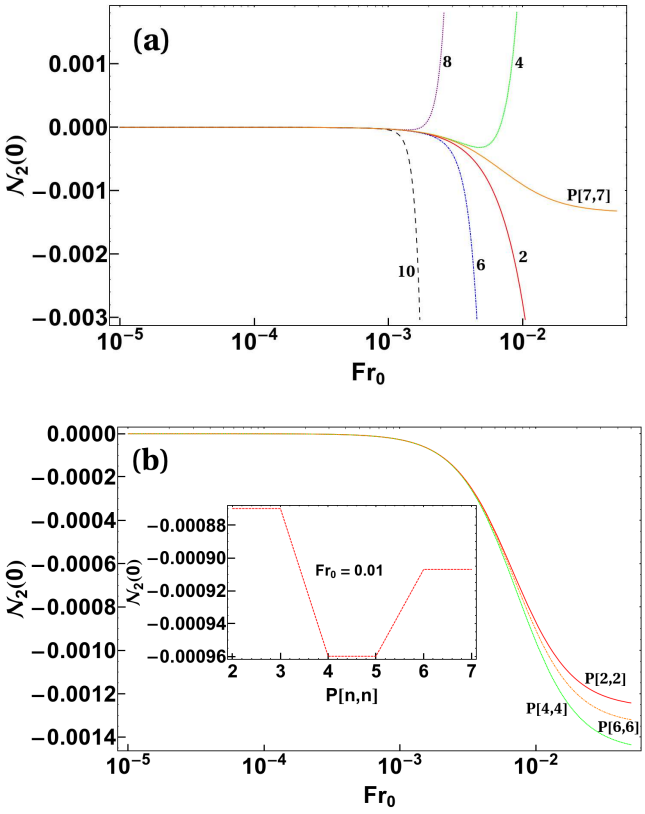

FIG. 12. Second normal-stress difference evaluated at channel centreline ($y = 0$) with Froude number Fr_0: (a) different order series solutions with their 7th-order Padé approximant and (b) comparison among three Padé approximants. Inset in panel b shows "diagonal" Padé approximants of different orders at $\mathrm{Fr}_0 = 0.01$.

The second-, fourth- and sixth-order diagonal Padé approximations for the tangential heat flux $q_x(0)$ in Eq. (97) are given by

$$\begin{aligned}
q_x^{[2,2]}(0) &\equiv \mathcal{P}_2^2\left[q_x(0)\right] = \frac{(5/8)\sqrt{\pi}\mathrm{Fr}_0}{1+656.53\pi\mathrm{Fr}_0^2},\\
q_x^{[4,4]}(0) &= \frac{(5/8)\sqrt{\pi}\mathrm{Fr}_0\left(1+\mathcal{C}_{q_x}^{(1)}\mathrm{Fr}_0^2\right)}{1+\mathcal{C}_{q_x}^{(2)}\mathrm{Fr}_0^2+\mathcal{C}_{q_x}^{(3)}\mathrm{Fr}_0^4},\\
q_x^{[6,6]}(0) &= \frac{(5/8)\sqrt{\pi}\mathrm{Fr}_0\left(1+\mathcal{C}_{q_x}^{(4)}\mathrm{Fr}_0^2+\mathcal{C}_{q_x}^{(5)}\mathrm{Fr}_0^4\right)}{1+\mathcal{C}_{q_x}^{(6)}\mathrm{Fr}_0^2+\mathcal{C}_{q_x}^{(7)}\mathrm{Fr}_0^4+\mathcal{C}_{q_x}^{(8)}\mathrm{Fr}_0^6},
\end{aligned} \tag{118}$$

with

$$\begin{aligned}
&\mathcal{C}_{q_x}^{(1)} = 503752.89\pi,\ \mathcal{C}_{q_x}^{(2)} = 504409.42\pi,\\
&\mathcal{C}_{q_x}^{(3)} = 2.95\times10^{8}\pi^2,\ \mathcal{C}_{q_x}^{(4)} = -639836.57\pi,\\
&\mathcal{C}_{q_x}^{(5)} = -1.52737\times10^{12}\pi^2,\ \mathcal{C}_{q_x}^{(6)} = -639180.04\pi,\\
&\mathcal{C}_{q_x}^{(7)} = -1.52783\times10^{12}\pi^2,\ \mathcal{C}_{q_x}^{(8)} = -9.62688\times10^{14}\pi^3.
\end{aligned} \tag{119}$$

Related comparisons for the tangential heat flux are displayed in Fig. 13 – only the 6th-order Padé-solution $\mathcal{P}_6^6[q_x(0)]$ is shown here but its lower-order counterparts,

$\mathcal{P}_2^2[q_x(0)]$ and $\mathcal{P}_4^4[q_x(0)]$, closely follow each other. Note that $\mathcal{P}_6^6[q_x(0)]$ is almost indistinguishable from the 3rd-order series solution up-to a value of $\mathrm{Fr}_0 = 0.01$, but deviates thereafter. Interestingly, all three Padé-solutions of $q_x(0)$ display a non-monotonic variation with Fr_0: it increases with increasing Fr_0, reaches a maximum and decreases thereafter.

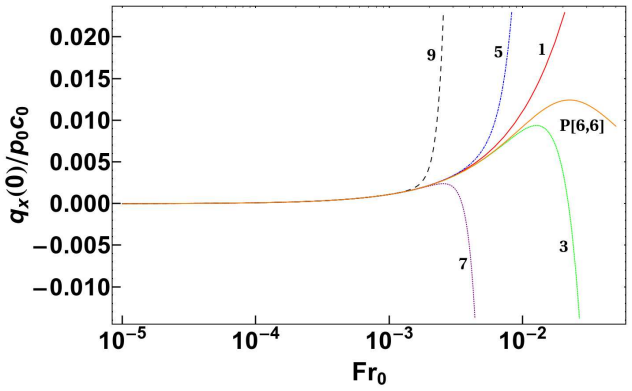

FIG. 13. Tangential heat flux evaluated at channel centreline ($y = 0$) with Froude number Fr_0: different order series solutions with their 6th-order Padé approximant.

For the centreline shear viscosity η_0 given in Eq. (96), its diagonal Padé approximations are given by

$$\begin{aligned}
\eta_0^{[3,3]} &\equiv \mathcal{P}_3^3[\eta_0] = \frac{5\sqrt{\pi}(1+24911.7\pi\mathrm{Fr}_0^2)}{8(1+25082.1\pi\mathrm{Fr}_0^2)}, \\
\eta_0^{[5,5]} &= \frac{(5/8)\sqrt{\pi}\left(1+\mathcal{C}_\eta^{(1)}\mathrm{Fr}_0^2+\mathcal{C}_\eta^{(2)}\mathrm{Fr}_0^4\right)}{1+\mathcal{C}_\eta^{(3)}\mathrm{Fr}_0^2+\mathcal{C}_\eta^{(4)}\mathrm{Fr}_0^4}, \\
\eta_0^{[7,7]} &= \frac{(5/8)\sqrt{\pi}\left(1+\mathcal{C}_\eta^{(5)}\mathrm{Fr}_0^2+\mathcal{C}_\eta^{(6)}\mathrm{Fr}_0^4+\mathcal{C}_\eta^{(7)}\mathrm{Fr}_0^6\right)}{1+\mathcal{C}_\eta^{(8)}\mathrm{Fr}_0^2+\mathcal{C}_\eta^{(9)}\mathrm{Fr}_0^4+\mathcal{C}_\eta^{(10)}\mathrm{Fr}_0^6},
\end{aligned} \tag{120}$$

with

$$\begin{aligned}
&\mathcal{C}_\eta^{(1)} = 1.929\times10^6\pi,\ \mathcal{C}_\eta^{(2)} = 3.96867\times10^{10}\pi^2, \\
&\mathcal{C}_\eta^{(3)} = 1.92917\times10^6\pi,\ \mathcal{C}_\eta^{(4)} = 4.00111\times10^{10}\pi^2, \\
&\mathcal{C}_\eta^{(5)} = -20810.2\pi,\ \mathcal{C}_\eta^{(6)} = 8.58213\times10^9\pi^2, \\
&\mathcal{C}_\eta^{(7)} = 1.5541\times10^{16}\pi^3,\ \mathcal{C}_\eta^{(8)} = -20639.8\pi, \\
&\mathcal{C}_\eta^{(9)} = 8.57434\times10^9\pi^2,\ \mathcal{C}_\eta^{(10)} = 1.55439\times10^{16}\pi^3.
\end{aligned} \tag{121}$$

Figure 14(a) shows a comparison of the 7th-order Padé-approximant $\mathcal{P}_7^7[\eta_0]$ of the shear viscosity with its series solutions at different orders. It is seen that the viscosity η_0 decreases with increasing Fr_0, reaches a minimum and increases thereafter, finally attaining a nearly constant value at $\mathrm{Fr}_0 \geq 0.01$ [see also the inset in Fig. 14(b)]. The main panel of Fig. 14(b) shows that the behaviour of the lower-order Padé-approximants ($\mathcal{P}_3^3[\eta_0]$ and $\mathcal{P}_5^5[\eta_0]$) can differ qualitatively from $\mathcal{P}_7^7[\eta_0]$. The differences among different-order Padé-approximants for η_0 might be due to the existence of a singularity of the underlying series solution for the shear viscosity. It appears that even a 10th-order series solution is not adequate to resolve the correct behaviour of η_0, and further higher-order terms in the series solution would be required to make a comparative study of $\mathcal{P}_7^7[\eta_0]$, $\mathcal{P}_9^9[\eta_0]$, etc. to arrive at a meaningful conclusion about the variation of shear viscosity with Fr_0. We remark here that the Chapman-Enskog solution for the viscosity of a sheared molecular gas does possess a branch-point singularity [30, 31] at a finite shear rate of order one, and the corresponding series solution was shown to be divergent but asymptotic [30].

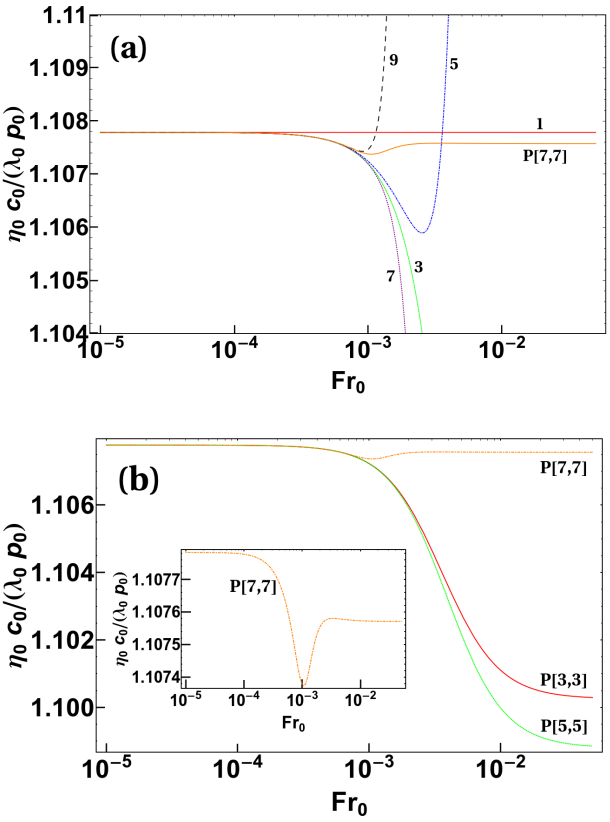

FIG. 14. Shear viscosity evaluated at channel centreline ($y = 0$) with Froude number Fr_0: (a) different order series solutions with their 7th-order Padé approximant and (b) comparison among three Padé approximants. Inset in panel *b* shows 7th-order Padé approximant.

On the whole, Figs. 11-14 confirm that the Padé approximations to the series solutions of each rheological field closely follow the leading-order series solution up-to a Froude number of $\mathrm{Fr}_0 \approx 10^{-3}$ and deviates with further increasing Fr_0. Each Padé approximant [Eqs. (114-120)] follows the next higher-order series solution for a little larger range of $\mathrm{Fr}_0 \approx 5\times10^{-3}$, however, the remaining higher-order solutions have a smaller range of validity in terms of Fr_0 – this indicates that the present series solutions are likely to be divergent but asymptotic. It is interesting to note that the Padé-approximant for each field retains the same sign of its leading-order series solution over a range of Fr_0 as found in the present work – therefore, each series solution [for example, Eqs. (88),

(90) and (101)] may be classified as "super-asymptotic" series [35]. A qualitative comparison of the present theoretical results can now be made with the recent DSMC simulations [20] of the acceleration-driven Poiseuille flow of a molecular gases. We have verified that the simulation data for all rheological fields have the same sign and similar variations with Froude number Fr_0 as that of our Padé approximants [Eqs. (114-120)]. Based on the present results, we may conclude that the Padé approximation to the 10th-order series solution extends the range of applicability of the respective series solutions in terms of Fr_0. Recall from Eq. (76), the Froude number is linearly proportional to the Knudsen number –therefore, the present Padé-approximated solutions are likely to be valid at large Knudsen numbers too.

VII. SUMMARY AND OUTLOOK

The gravity-driven Poiseuille flow of hard-sphere gases flowing through a channel has been analysed using a perturbation expansion of the velocity distribution function in powers of the strength of gravitational acceleration (the Froude number $\mathrm{Fr}_0 = g\lambda_0/c_0^2$, where λ_0 is the mean-free path and c_0 is the thermal speed, both evaluated at the center of the channel) by retaining terms upto tenth-order in Fr_0. The resulting power-series solutions hold only around the channel centerline since the wall-effects have been neglected in the present analysis. Rarefaction effects (e.g. the bimodal shape of the temperature profile, normal stress differences, tangential heat flux, etc) have been critically analysed using the presently derived high-order series solutions. It is found that the temperature bimodality [$\triangle T = (T_{\max}/T_0 - 1)$, where T_0 is the temperature at the channel centerline and $T_{\max}$ is the maximum temperature that occurs away from the channel center] and all transport coefficients show oscillating behaviour for Froude numbers greater than 10^{-3}, and just adding further higher-order terms does not help to obtain converged solution. Similar type of oscillatory behaviour with increasing perturbation parameter Fr_0 has been confirmed also for (i) the first normal-stress difference, (ii) second normal-stress difference, (iii) tangential heat flux and (iv) shear viscosity. The analyses of the present series solutions revealed that the coefficients in each series expression of $\mathcal{N}_1(0)$, $\mathcal{N}_2(0)$, $q_x(0)$ and $\eta(0)$ alternate in signs with increasing order of Fr_0, indicating possible divergent nature of the adopted series expansion.

The Padé approximation method has been employed to understand the convergence of the series solutions. The Padé approximants of different order have been obtained for $\mathcal{N}_1(0)$, $\mathcal{N}_2(0)$, $q_x(0)$ and $\eta(0)$, with each field being evaluated at the channel centreline. It is found that the Padé-approximants for two normal-stress differences $\mathcal{N}_1(0)$ and $|\mathcal{N}_2(0)|$ show increasing trends with increasing Fr_0 as confirmed in Fig. 4 and Fig. 5, which also agrees qualitatively with the recent DSMC simulations of Ref. [20]. The present analysis indicates that the "diagonal" Padé approximation yields accurate solution for each field for a much larger range of Froude numbers up-to $\mathrm{Fr}_0 \approx 10^{-2}$. Except for shear viscosity, the Padé approximants for the remaining rheological fields [$\mathcal{N}_1(0)$, $\mathcal{N}_2(0)$ and $q_x(0)$] point toward the asymptotic character of the underlying series solution. We conclude that the present series solutions must be Padé-approximated to make it useful at higher values of Froude number.

The current approach of testing high-order series solutions in terms of their Padé-approximants has been extended to study the analogous gravity-driven flow of a heated granular gas [39]. For the latter case, the inelasticity-dependence of the higher-order solutions for both hydrodynamic and rheological fields are found to be fundamentally different from their leading-order counterparts depending on the value of the Froude number. Moreover, it has also been confirmed [39] that the present Padé-approximants provide a useful guide (or, benchmark) to decide the "order" of series solutions that must be retained to obtain accurate solutions for the related granular Poiseuille flow – these results will be discussed in a future publication. Another interesting future work would be to determine the solutions of 13-moment extended hydrodynamic equations [40–42] with appropriate boundary conditions for Poiseuille flow and compare them with the present Padé-approximants in the bulk region of the channel.

ACKNOWLEDGEMENTS

A part of this manuscript was written when M.A. was visiting the Kavli Institute for Theoretical Physics (UC Santa Barbara) to participate in the KITP Program on "Physics of Dense Suspensions", and was supported in part by the National Science Foundation under Grant No. NSF PHY11-25915. We are grateful to Prof. Andrés Santos for detailed comments on the draft manuscript; R.R. sincerely thanks Dr. M. H. L. Reddy for suggestions and help in editing a part of the text of a previous draft.

[1] J. L. M. Poiseuille, Recherches experimentales sur le mouvement des liquides de nature differente dans les tubes de tres petits diametres, (1847).
[2] G. Hagen, Uber die Bewegung des Wassers in engen cylindrischen Rohren, Annalen der Physik. **122**, 423 (1839).
[3] M. Knudsen, Die Gesetze der Molekularstromung und der inneren Reibungsstromung der Gase durch Rohren, Ann. Phys. **28**, 75 (1909).
[4] C. Cercignani and C. Daneri, Flow of a rarefied gas between two parallel plates, J. Appl Phys. **76**, 1399 (1963).
[5] M. Tij and A. Santos, Perturbation analysis of a stationary non-equilibrium flow generated by external force,

J. Stat. Phys. **76**, 1399 (1994).
[6] M. Alaoui and A. Santos, Poiseuille flow driven by an external force, Phys. Fluids. A **4**, 1273 (1992).
[7] M. Tij, M. Sabbane, and A. Santos, Nonlinear Poiseuille flow in a gas, Phys. Fluids **10**, 1021 (1998).
[8] F. J. Uribe and A. L. Garcia, Burnett description of plane Poiseuille flow, Phys. Rev. E **60**, 4063 (1999).
[9] S. Hess and M. M. Mansour, Temperature profile of a dilute gas undergoing a plane Poiseuille flow, Physica A **272**, 481 (1999).
[10] D. Risso and P. Cordero, Generalized hydrodynamics for a Poiseuille flow: theory and simulations, Phys. Rev. E **58**, 546 (1998).
[11] M. Tij and A. Santos, Non-Newtonian Poiseuille flow of a gas in a pipe, Physica A **289**, 336 (2001).
[12] K. Aoki, S. Takata, and T. Nakanishi, Poiseuille-type flow of a rarefied gas between two parallel plates driven by a uniform external force, Phys. Rev. E **65**, 026315 (2002).
[13] M. Sabbane, M. Tij, and A. Santos, Maxwellian gas undergoing a stationary Poiseuille flow in a pipe, Physica A **327**, 264 (2003).
[14] M. Tij and A. Santos, Poiseuille flow in a heated granular gas, J. Stat. Phys. **117**, 901 (2004).
[15] A. Santos and M. Tij, Gravity-driven Poiseuille Flow in Dilute Gases. Elastic and Inelastic Collisions, In *Modelling and Numerics of Kinetic Dissipative Systems*, edited by L. Pareschi, G. Russo, and G. Toscani (Nova Science Publishers, New York, 2006), pp. 53-67.
[16] M. M. Mansour, F. Baras, and A. L. Garcia, On the validity of hydrodynamics in plane Poiseuille flows, Physica A **240**, 255 (1997).
[17] K. P. Travis, B. D. Todd, and D. J. Evans, Poiseuille flow of molecular fluids, Physica A **240**, 315 (1997).
[18] B. D. Todd and D. J. Evans, Temperature profile for Poiseuille flow, Phys. Rev. E **55**, 2800 (1997).
[19] M. Alam, A. Mahajan, and D. Shivanna, On Knudsen-minumum effect and temperature-bimodality in dilute granular Poiseuille flow, J. Fluid Mech. **782**, 99 (2015).
[20] R. Gupta and M. Alam, Hydrodynamics, wall-slip, and normal-stress differences in rarefied granular Poiseuille flow, Phys. Rev. E **95**, 022903 (2017).
[21] R. Gupta and M. Alam, Disentangling the role of athermal walls on the Knudsen paradox in molecular and granular gases, Phys. Rev. E **97**, 012912 (2018).
[22] G. A. Bird, *Molecular Gas Dynamics and the Direct Simulation Monte Carlo of Gas Flows* (Clarendon, Oxford, 1994).
[23] P. L. Bhatnagar, E. P. Gross, and M. Krook, A model for collision processes in gases. I. small amplitude processes in charged and neutral one-component systems, Phys. Rev. **94**, 511 (1954).
[24] A. Santos, Transport coefficients of d-dimensional inelastic Maxwell models, Physica A **321**, 442 (2003).
[25] S. Chapman and T. G. Cowling, *The Mathematical Theory of Non-Uniform Gases* (Cambridge University Press, Cambridge, UK, 1970).
[26] N. Sela and I. Goldhirsch, Hydrodynamic equations for rapid flows of smooth inelastic spheres, up-to Burnett order, J. Fluid Mech. **361**, 41 (1998).
[27] M. Alam and S. Luding, Non-Newtonian granular fluid: Simulation and theory, In *Powders and Grains*, edited by R. Garcia-Rojo, H. J. Herrmann and S. McNamara (Balkema, The Netherlands, 2005), pp. 1141-1145.
[28] M. N. Kogan, *Rarefied Gas Dynamics* (Plenum, New York, 1969).
[29] There are two Supplemental documents at [http:// ..]. See Supplemental Material I for exact expressions for distribution functions beyond second-order [$\Phi^{(3)}$, $\Phi^{(4)}$, $\cdots$, $\Phi^{(10)}$].
Supplemental Material II at [http:// ..] contains Appendices A and B; Appendices B.1 ["Streamwise velocity and shear-rate profiles"], B.2 ["Coefficients for temperature profile"], B.3 ["Coefficients for P_{xx}, P_{yx} and p profiles"], and B.4 ["Coefficients for heat-flux (q_x and q_y) profiles"] are given in Sec. B of Supplemental Materials II.
[30] A. Santos, J. J. Brey, and J. W. Dufty, Divergence of the Chapman-Enskog expansion, Phys. Rev. Lett. **56**, 1571 (1986).
[31] A. Santos, Does the Chapman–Enskog expansion for sheared granular gases converge?, Phys. Rev. Lett. **100**, 078003 (2008).
[32] N. V. Brilliantov and T. Pöschel, Breakdown of the Sonine expansion for the velocity distribution of granular gases, Europhys. Lett. **74**, (2006).
[33] S. H. Noskowicz, O. Bar-Lev, D. Serero, and I. Goldhirsch, Computer-aided kinetic theory and granular gases, Europhys. Lett. **79**, (2007).
[34] H. Padé, Sur la Representation Approchee d'une Fonction par des Fractions Rationelles, Ann. de l'Ecole Normale Superieure suppl, pp. 1-93 (1892).
[35] C. M. Bender and S. A. Orszag, *Advanced Mathematical Methods for Scientists and Engineers: Asymptotic Methods and Perturbation Theory* (Springer, New York, 1999).
[36] G. A. Baker Jr and P. Graves-Morris, *Padé Approximants* (Cambridge University Press, New York, 1996).
[37] A. Pozzi, *Applications of Padé Approximation Theory in Fluid Dynamics* (World Scientific Publishing, Singapore, 1994).
[38] C. Cercignani, *The Boltzmann Equation and Its Applications* (Springer, New York, 1988).
[39] R. Rongali and M. Alam, Bulk hydrodynamics and rheology of a gravity-driven heated granular gas: competition between inelasticity and forcing, Preprint (2018)
[40] S. Saha and M. Alam, Non-Newtonian stress, collisional dissipation and heat flux in the shear flow of inelastic disks: a reduction via Grad's moment method, J. Fluid Mech. **757**, 251-296 (2014).
[41] S. Saha and M. Alam, Normal stress differences, their origin and constitutive relations for a sheared granular fluid, J. Fluid Mech. **795**, 549-580 (2016).
[42] S. Saha and M. Alam, Revisiting ignited-quenched transition and the non-Newtonian rheology of a sheared dilute gas-solid suspension, J. Fluid Mech. **833**, 206-246 (2017).